Identification of microscopic uranium particles using fission tracks in solid detectors

Neutron Physics Laboratory - Nuclear analytical methods with neutrons

Jan Lorincik

Proposal ID

332

Report regarding proposal " **Identification of microscopic uranium particles using fission tracks in solid detectors"**

J. Lorinčík, K. Sihelská, K. Řezanková, F. Sus, Vl. Strunga, J. Kučera

The goals of this project were (A) the study of the number of fission tracks as a function of enrichment and size of U-particles, (B) the optimization of the fission track (FT) procedure for higher reproducibility, robustness, and accuracy.

A quantitative relation between the U-particle enrichment, size, and the number of FTs was used in the following form *[1]*: $N_T = N_{235} \cdot \sigma_f \cdot \varepsilon \cdot t \cdot \phi_{therm}$ … (1) , where N_T denotes the number of fission tracks; N_{235}, the number of ^{235}U atoms in a particle; σ_f, the fission cross section for ^{235}U [586 b]; ε, the registration efficiency (0,4); t, the irradiation time [120 s]; Φ_{therm}, the flux of thermal neutrons [3,2 x 10^{13} $cm^{-2}s^{-1}$]. Then, N_{235} can be obtained from $N_{235} = 3 \cdot (\rho_{U3O8} \cdot V_P)/M_{U3O8} \cdot N_A \cdot A_{235}/100$ … (2), where ρ_{U3O8} is U_3O_8 particle density [8,3 g/cm^3], V_P volume of the particle [cm^3], M_{U3O8} the molar mass of U_3O_8 [842,1 g/mol], N_A the Avogadro's constant, A_{235} the enrichment [%]. Constant 3 in eq. (2) corresponds to the number of U atoms in U_3O_8 molecule. Since SEM images can provide only areas of 2D projections (characterized by equivalent circle diameter – d_{ECD}) of 3D shapes of particles, the geometry models, e.g. sphere, cylinder, cube must be used for *Vp* estimation.

For experimental work, standard reference materials of U_3O_8 were used: CRM 129-A (NU), CRM 010 (1% ^{235}U enriched), CRM 030-A (3% ^{235}U enriched). Then FT sample assemblies (see more detail in reports of project CANAM:ID241) were prepared and irradiated in the reactor LVR-15 with irradiation parameters specified above. After etching of the Lexan detectors, optical images were made (see Fig. 1 a-c) and the FTs manually counted. The comparison of theoretical estimates and experimental data (lines vs. data points) is in Fig. 1 d.

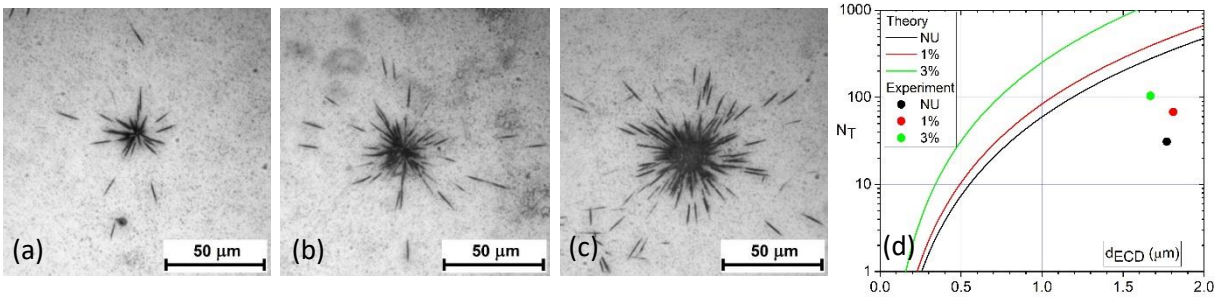

Figure 1.Optical images of FTs corresponding to U_3O_8 particles of NU (a),1 %U (b),and 3%U (c) [2]. Number of registered FTs in the images (a)-(c) for NU, 1%U, 3%U is 31, 68, 104, resp. (d) Comparison of experimental values (circle symbols) and theoretical estimates (full lines) based on equations (1) and (2) for spherical geometry model ($V_P = \pi/6 \cdot d_{ECD}^3$).

In parallel to the above study, large effort has been spent on improvement of the FT procedure. This goal has been achieved by (i) reconfiguration of the fiducial marks for better particle position precision, (ii) addition of sticky collodion for better particle adhesion, (iii) redesigning of the FT sample assembly for simpler and more reliable manipulation, (iv) employing new optical microscope with motorized stage for automated creation of compound photos of large areas of the Lexan detector, and (v) implementing efficient coordinate transformation algorithm for transfer of particle coordinates between instruments.

In summary, the dependence of the number of FTs on the particle enrichment and size has been investigated both theoretically and experimentally. There is a discrepancy between the theoretically predicted numbers of FTs and the counts of FTs obtained from the experiment. A combined effect of overestimated values of neutron fluences, material density, and FT registration efficiency could have been responsible for that. More experiments are needed to support that explanation and to provide more accurate data for theoretical predictions.

The main outcome of this project is substantial improvement of the FT procedure, which achieved the readiness level that allowed for the proficiency testing for nuclear safeguards.

[1] O. Stetzer, et al, . Nucl. Instr. Meth. Phys. Res. A525 (2004), pp. 582-592.
[2] S. Konegger-Kappel, et al https://www.iaea.org/sites/default/files/19/07/cn-267-book-of-abstracts.pdf, CN267-226, pp.228.

Testing of the Chamber for Light Ion Detection

Laboratory of Cyclotron and Fast Neutron Generators

Martin Ansorge

Proposal ID

460

Final report regarding the proposal „Testing of the Chamber for Light Ion Detection“

M. Ansorge, J. Novák, M. Majerle, Nuclear Physics Institute of the CAS, Rez, Czech Republic

Motivated by gas production in construction materials of future fusion-related facilities as well by the basic research of nuclear reactions new detection system is under development at NPI of the CAS in recent years. The chamber is equipped with dE-E Si-detector telescopes for distinguishing between charged particle types. The CAEN V1730 digitizer is used for data acquisition. In figure 1 the vacuum chamber is shown during the preparations on the on-beam tests of electronics.

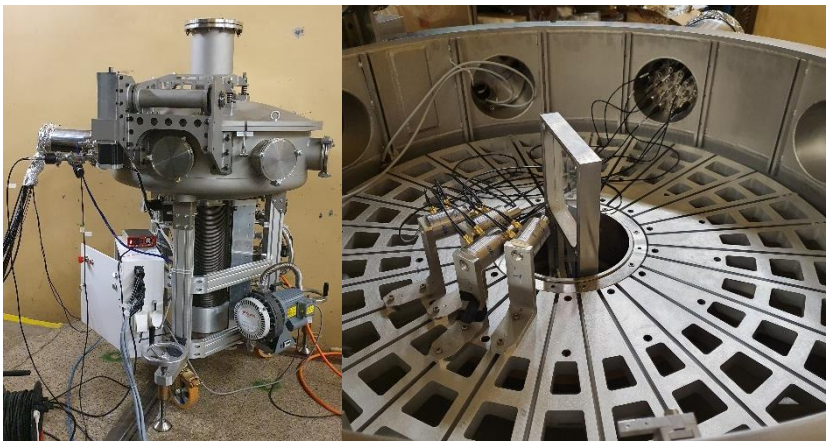

Figure 1 shows the typical experimental setup during the on-beam tests. Telescopes with Si-detectors are placed around the central sample-holder.

Days-lasting measurements with several irradiations of PE, C, Al samples were successfully performed, and the acquisition chain was finalized. The signal-noise ratio of detectors was suppressed by additional electro-magnetic shielding of preamplifiers. The detection system exhibited a good ability to measure the energy distribution of charged particles and the reasonable separation of particle types was achieved, see figure 2. It was shown that the time resolution of detected events is sufficient for usage the ToF technique and ToF method was successfully implemented.

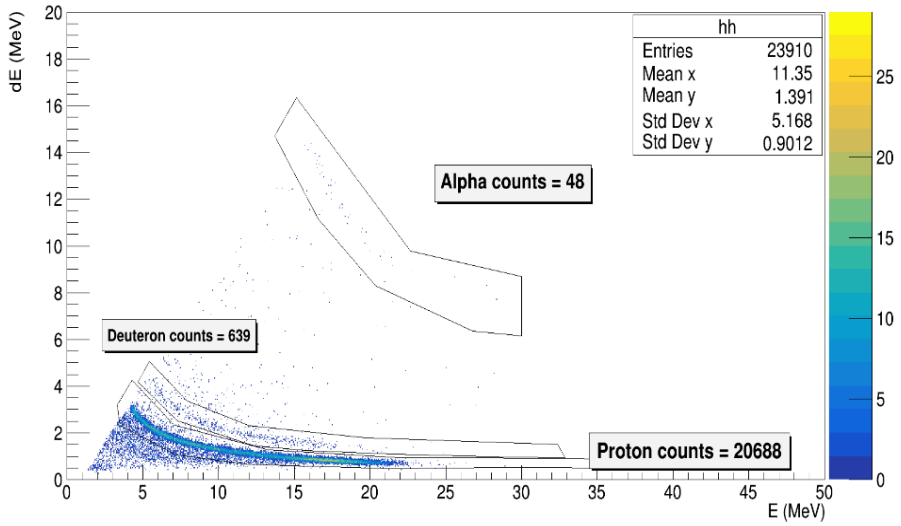

Figure 2 shows the dE-E plot of detected charged-particle-events from the six hours long irradiation of the PE target foil (thickness of 180 um, diam 3 cm) which was mounted into the central position of the vacuum chamber.

Many challenges are still ahead of us but the measurements that have been made provided us with very useful data which are used as feedback for detection electronics enhancements as well as for the development of a comprehensive software framework for data analysis in measurements of double-differential cross-sections for reactions (n, cp) induced by fast neutrons.

Micro-PIXE for quantitative mapping of metal concentration in O. glaberrima and O. sativa riceplants

Laboratory of Tandetron

Alassane Alassane

Proposal ID

397

Multi-elemental analysis of roots and leaves from Oryza glaberrima rice plants at vegetative stage of growth by combined PIGE, RBS, PIXE and GC-TDS methods

S. Fernandes[a,*], A. Traoré[b], O. Fleury[b], V. Havránek[a], J. Kučera[a], A. Ndao[b]
[a]Nuclear Physics Institute CAS, v.v.i., 250 68, Husinec - Řež, Czech Republic
[b]Institute for Applied Nuclear Technology, Cheikh Anta Diop University, Dakar, Senegal

This study aims at understanding the bioaccumulation and transport mechanisms of both micro- and macronutrients in the leaves and roots of African rice *Oryza glaberrima* Steud (OG) plants cultivated in Senegal during the wet season at the vegetative stage of growth to determine the translocation factors from roots to leaves and to evaluate the suitability of OG rice plants for phytoremediation. A comparative analysis of the elemental composition of roots and leaves of OG plants, provided information on the bioaccumulation of nutrients necessary for plant growth which can become detrimental if their toxicity level is reached. The elemental analysis of basic nutrients (C, H, O), macronutrients (N, P, K, Ca, Mg and S) and micronutrients (Cl, Fe, Cu, Mn, Ni and Zn) in the OG roots and leaves was made possible by several elemental analytical techniques (PIGE, RBS, PIXE and GC-TDS). All methods were validated by analysis of pure substances and certified reference materials. The high accumulation rate of Cu (5 x), Al (4 x) and Fe (~ 2 x) in the OG rice roots relative to the leaves indicates the existence of low translocation factors for these metals from root to leaves probably due to the existence of plant mechanisms to limit their transport and to preferentially accumulate Si (% mass: 5.2 ± 0.5) in the rice leaves. The high accumulation rates of Mn, Ni, Rb and Cr "heavy" metals in the OG leaves relative to the roots, shows that these can be partially removed from soil through phytoextraction processes by harvesting the shoot tissues.

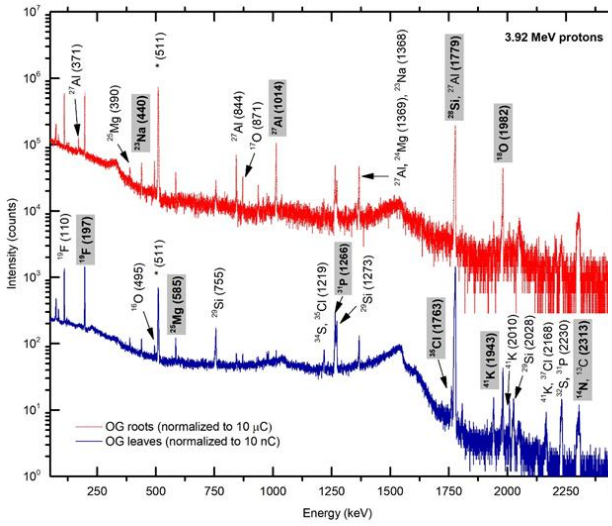

Figure 2 Normalized γ-ray spectrum for OG leaves and roots at 3.92 MeV protons. The γ-energy reference peak used for isotopic quantification is indicated inside grey boxes and highlighted in bold

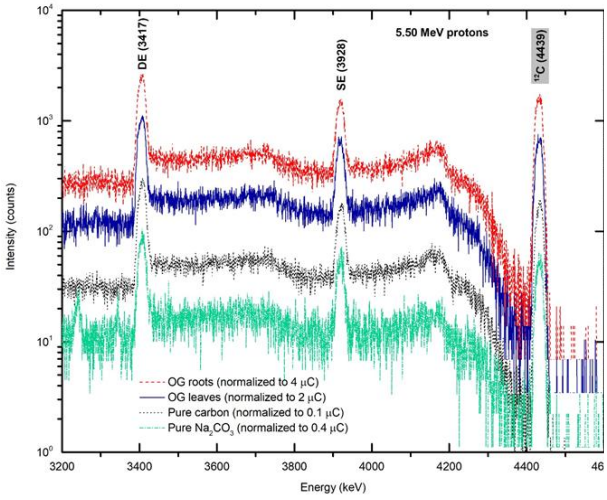

Figure 1 Detail of the normalized γ-ray spectrum of OG leaves and roots, and standard materials C and Na_2CO_3 at 5.5 MeV protons showing the reaction $^{12}C(p,p_1\gamma)^{12}C$ at 4439 keV and its single and double escape peaks.

The determination of the elemental composition of cultivated soil and OG rice stems and grains is necessary to obtain the translocation factors of nutrient and non-nutrient into different plant organs from soil to root and from leaves to grains for characterization of their transport into the plant cells. The analysis of the OG rice grains is needed to testify that all the potential toxic elements identified in this study, and other heavy metals such as As, Sb, Cd, Hg and Pb, known to be absorbed by the plant biomass, were not accumulated to toxic levels for human consumption to ensure food security in West Africa.

[1] S. Bado et al. NIM B 371 (2016) 407 - 412.

Characterization of Residual Stresses Distribution in Laser Cladded H13 tool steel

Neutron Physics Laboratory - Neutron diffraction

Karel Trojan

Proposal ID

461

Report regarding proposal "Characterization of Residual Stresses Distribution in Laser Cladded H13 Tool Steel"

K. Trojan [1,a], D. Canelo-Yubero[2], J. Čapek [1], N. Ganev [1]

[1] Department of Solid State Engineering, Faculty of Nuclear Sciences and Physical Engineering, CTU in Prague, Trojanova 13, 120 00 Prague 2, Czech Republic
[2] Department of Neutron Physics, Nuclear Physics Institute, ASCR, v.v.i., 25068 Řež, Czech Republic
[a] karel.trojan@fjfi.cvut.cz

Laser cladding was carried using a IPG 3kW Yt:YAG fibre laser and powder of the AISI H13 tool steel. Five-layer sample was formed from six and seven overlapping beads on the substrate made from AISI H11 tool steel. The state of residual stress and the dependence of the FWHM parameter were described using neutron diffraction in the middle of the sample in the plane perpendicular to cladding.

It was found from the measured residual stresses in three different sample orientations (see Fig. 1) that the greatest gradient of residual stresses (RS) is in the direction normal to the surface (N – normal direction). According to the literature study [1, 2], the maximum residual stresses are located 4 mm below the surface and compressive stresses prevail in the T direction. The substrate, on the other hand, exhibits tensile residual stresses. According to our results in the clad itself in the T direction, tensile RS predominate, on the contrary, in the substrate compressive RS with one maximum of tensile RS approximately 3 mm below the surface of the substrate were determined.

Laser deposition of the H13 tool steel showed a great application potential. The obtained results will help to understand the development of residual stresses within the thickness of the newly formed material. This knowledge can be used to design a procedure for laser beam deposition of larger volumes.

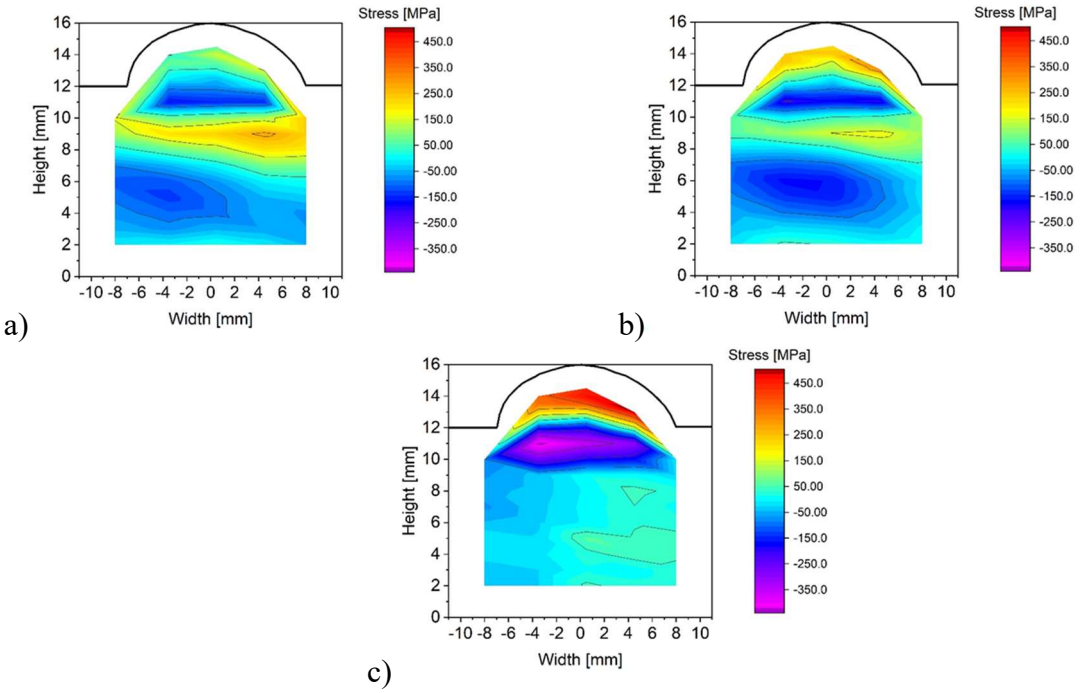

Fig. 1: Map of bulk residual stresses in the cross section of the clad in a) L, b) T and c) N direction.

Reference

[1] Cottam, R., Wang, J., & Luzin, V. (2014). Characterization of microstructure and residual stress in a 3D H13 tool steel component produced by additive manufacturing. Journal of Materials Research, 29(17), 1978-1986. doi:10.1557/jmr.2014.190

[2] Bailey, N., Katinas, C., & Shin, Y. (2017). Laser direct deposition of AISI H13 tool steel powder with numerical modeling of solid phase transformation, hardness, and residual stresses. Journal of Materials Processing Technology, 247, 223-233.

Effect of high LET radiation on specific interaction of proteins with DNA.

Laboratory of Tandetron

Marie Davidkova

Proposal ID

17

Report regarding proposal " Effect of high LET radiation on specific interaction of proteins with DNA."

M. Davídková, A. Michaelidesová, J. Vachelová, Nuclear Physics Institute of the CAS, Řež, Czech Republic

External microbeam of Tandetron accelerator has been applied to study response of normal human neonatal skin fibroblasts. Cells were grown on Mylar foils or Lumox dishes with Teflon bottom membrane (Sarstedt) in Dulbecco's Modified Eagle's medium (Sigma-Aldrich) supplemented with 15% fetal bovine serum (FBS—BIOSERA) and standard antibiotics (100 U/ml penicillin and 0.1 mg/ml streptomycin, Sigma-Aldrich). Experimental setup is presented in Figure 1. Cell monolayers were irradiated by 1, 2 and 3 Gy of 1.1 MeV protons. Biological response of fibroblasts to acute irradiation was assessed using Muse cell analyzer (Merck Millipore).

Relative proportion of of living, early and late apoptotic cells in cell population was followed using Muse Annexin V & Dead Cell Kit (Luminex). The results obtained immediately after irradiation, 9 and 12 days postirradiation. No dependence on absorbed dose has been detected.

To monitor changes in enzyme activity in living cells, the enzymes catalase (CAT), superoxide dismutase (SOD) and glutathione peroxidase (GPx), which decompose hydrogen peroxide into water and oxygen, were selected. These enzymes do not interact with specific DNA sequences, but respond to oxidative stress in cells. Enzyme activity was determined by colorimetric detection in cells irradiated with increasing doses of gamma radiation or protons.

PCR method was newly introduced in the laboratory. The activity of genes key for the repair of radiation DNA damage was determined in irradiated samples (repair of single DNA strand breaks - Parp1; homologous recombination of DNA double breaks - Rad51, Rad52; non-homologous joining of DNA strands - Ku80, Artemis F, DNA-PKcs, Ligase IV, XRCC4), regulation of apoptosis and cell cycle (bax, bcl2, Birc5, p21 and p16), response to oxidative stress (CAT, SOD1, SOD2, GPx-1, GPx-4), and fibroblast function (IL- 6). Gene activity was monitored depending on the radiation dose and quality (gamma radiation, protons, alpha particles). The used techniques did not detect any changes in the functionality of proteins in irradiated cells (eg. active enzymes for repairing DNA damage in senescent cells, active proapoptotic enzymes in surviving cells, negative changes in antioxidant enzyme activity with increasing radiation dose, etc.). The study should be repeated and extended for other cell lines.

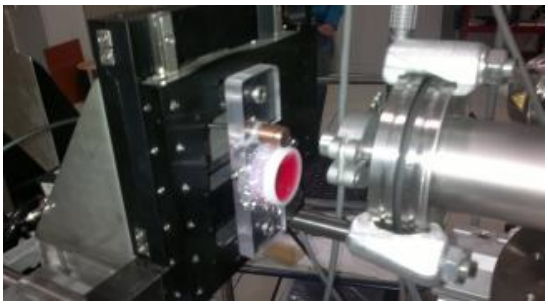

Figure: Experimental setup for irradiation of cell monolayers.

IMMEDIATELY AFTER IRRADIATION				
Dose (Gy)	0	1	2	3
Live	76.85	62.85	80.15	78.75
Early apop.	18.55	32.45	16.2	18.35
Late apop/dead	4.25	4.5	3.2	2.75
Derbis	0.35	0.2	0.45	0.15
Total apop.	22.8	39.95	19.4	21.1

9 DAYS POST IRRADIATION				
Dose (Gy)	0	1	2	3
Live	50.6	53.6	52.55	50.1
Early apop.	45.2	43	44.4	46.2
Late apop/dead	3	2.75	2.75	3.35
Derbis	1.2	0.65	0.3	0.35
Total apop.	48.2	45.75	47.15	49.55

12 DAYS POST IRRADIATION				
Dose (Gy)	0	1	2	3
Live	49.9	49.05	39.75	41.85
Early apop.	44.15	44.55	55.45	53.7
Late apop/dead	5.2	5.35	4.05	3.85
Derbis	0.75	1.05	0.75	0.6
Total apop.	49.35	49.9	59.5	57.55

Table: Proportion of living, early and late apoptotic cells in cell population irradiated by 1.1 MeV protons.

Advanced organic-inorganic nanostructures

Laboratory of Tandetron

Vladimir Cech

Proposal ID

466

Report on the project "Advanced organic-inorganic nanostructures"

V. Cech, Inst. Mater. Chem., Brno Univ. Technol., Brno, Czech Republic
A. Romanenko, A. Mackova, Nucl. Physics Inst., Rez, Czech Republic

The main task of the proposed experiment was to provide an elemental analysis of polymer-like hydrogenated amorphous carbon-silicon (a-CSi:H) films using RBS and ERDA. The polymer-like a-CSi:H films were deposited from the tetravinylsilane (TVS) precursor by continuous wave (low-pressure plasma-enhanced chemical vapor deposition, LP PECVD) at an extremely low RF power of 0.2 W. These films were found to be unstable under ambient conditions and subject to post-deposition oxidation. The polymer-like film must therefore be overcoated with a 6-8 nm thick barrier layer to protect it and prevent degradation. A compact a-CSi:H film with a density of 2.0 g/cm^3 was successfully used as a barrier (XPS depth profiling), which was deposited from the TVS/Ar mixture by pulsed plasma at 25 W. To optimize the elemental analysis and increase the sensitivity to light elements, the films were deposited only on glassy carbon as a substrate. Further ERDA measurements showed a problem with the sputtering of polymer-like film and therefore it was necessary to optimize the ERDA charge per measurement. The areas affected by irradiation are visible to the eye as the charge was gradually reduced by 7.4, 3.7, 1.48, and 0.74 μC per measurement, see Fig. 1.

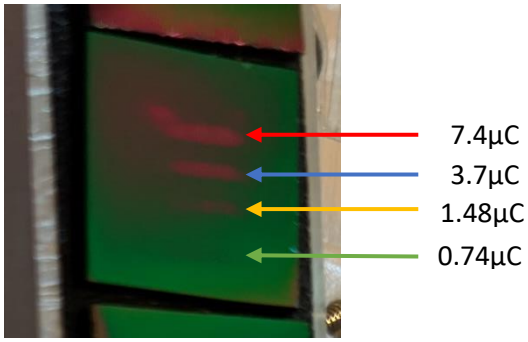

Fig. 1. Photo of the polymer-like film after testing in (a) ERDA geometry and (b) RBS measurements.

Although the ERDA charge was only 0.37 μC per measurement and 20 consecutive measurements were made at one location (the angle of incidence was 75°), the film on the surface is subject to changes during irradiation. It was found that both the thickness and the hydrogen concentration are reduced. Using an RBS charge of 0.74 μC per measurement (the angle of incidence was 7°), 10 measurements in a row were performed at one location. The final ERDA and RBS spectra corresponding to a charge of 0.74 μC can be seen in Fig. 2. The composition of the film (atomic [mass] concentration) is as follows: Si 7[28.2]%, C 37[63.8]%, H 56[8]%. The film thickness of 6200×10^{15} at/cm^2 corresponds to a thickness of 591 nm (measured by spectrometric ellipsometry) when a density of 1.2 g/cm^3 is used (GISA program).

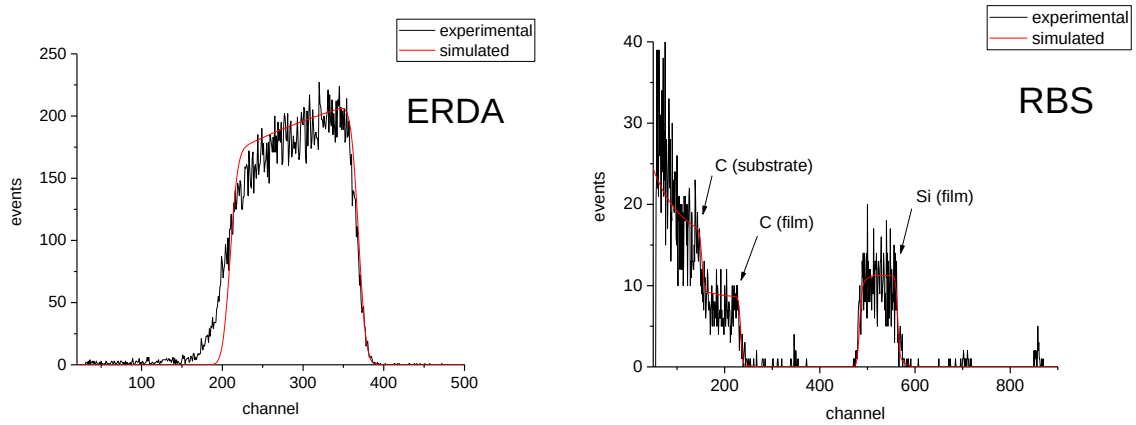

Fig. 2. ERDA and RBS spectra of polymer-like film corresponding to a charge of 0.74 μC.

Careful analysis of polymer-like a-CSi:H films is important for the further construction of layered nanostructures combining the polymer-like and oxygen bound a-CSiO:H films.

Preparation, modification and characterization of materials by radiation

Laboratory of Tandetron

Marie Davidkova

Proposal ID

18

Report regarding proposal "Preparation, modification and characterization of materials by radiation"

M. Davídková, A. Michaelidesová, J. Vachelová, Nuclear Physics Institute of the CAS, Řež, Czech Republic
L. Bačáková, M. Vandrovcová, Institute of Physiology of the CAS, Prague, Czech Republic

External microbeam of Tandetron accelerator has been applied to study response of normal cell line to ionizing radiation of different quality. Biological efficiency of proton and alpha particle beams was compared. Human normal neonatal skin fibroblasts were irradiated by 1.1 MeV proton and 2.5 MeV alpha particle beams. Cells were grown on Lumox dishes with Teflon bottom membrane (Sarstedt) in Dulbecco's Modified Eagle's medium (Sigma-Aldrich) supplemented with 15% fetal bovine serum (FBS—BIOSERA) and standard antibiotics (100 U/ml penicillin and 0.1 mg/ml streptomycin (Sigma-Aldrich). Confluent cell monolayers were irradiated by doses 0.5, 1, 3 and 5 Gy of protons or alpha particles. Biological response of fibroblasts to acute irradiation was assessed using clonogenic and micronuclei formation assays.

Colony formation analysis as survival test was performed for 250 or 500 cells per dish growing during 14 days in standard conditions for cell cultivation. Photo of dishes with colonies obtained by seeding of 500 cells per dish irradiated by 0, 0.5, 1, 3, 5 Gy of alpha particle beam is shown on figure 1a.

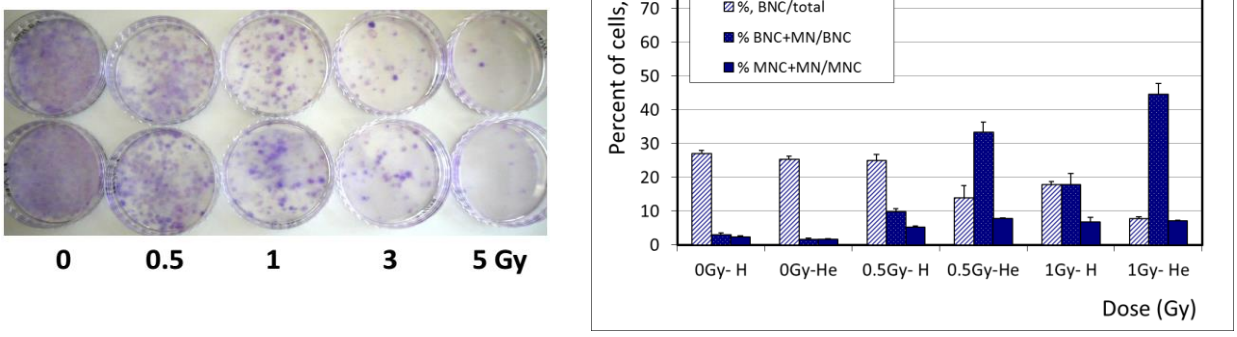

a) b)

Figure 1: a) colony formation of human fibroblasts irradiated by alpha particles. b) micronuclei formation in human neonatal fibroblasts after irradiation by different doses of protons and alpha particles.

Results of micronuclei formation test for alpha and proton irradiation at the same dose range show that alpha particles cause heavier DNA damage. For instance, 45% binuclear cells (BNC) containing micronuclei (MN) has been observed after irradiation by 1 Gy of alpha particles in comparison to about 18% BNC+MN after proton irradiation (figure 1b). Higher doses of alpha irradiation induced also cell senescence, which was not observed in proton-irradiated cells. Further increase of MN formation after 3-5 Gy alpha-irradiation was stopped by the replicative senescence in alpha-irradiation treated cells but not in proton-irradiated.

This pilot study was supported by the project of the Czech Science Foundation No. P108/12/G108.

Crystal and magnetic structure of La18M3Co28 (M=Mg,In,Cd)

Neutron Physics Laboratory - Neutron diffraction

Vitalii Shtender

Proposal ID

467

Report regarding proposal “Crystal and magnetic structure of $La_{18}M_3Co_{28}$ (M=Mg,In,Cd)”

V. Shtender, M. Sahlberg, Uppsala University, Sweden
Instrument responsible: C. Hervoches P. Beran, Nucl. Physics Inst., Rez, Czech Republic

The aim was to investigate crystal as well as magnetic structures of the $La_{18}M_3Co_{28}$ (M = Mg, Cd and In) compounds. There was need to confirm the XRD first results on incommensaturate crystal structures and resolve their different magnetic properties.

Neutron powder diffraction experiments were performed on different samples of general $La_{18}Mg_3Co_{28}$ composition at 298 K using the MEREDIT instrument. The motivation for the experiments was to investigate the possible large displacement of Mg.

The extracted data is still under evaluation but preliminary results propose modulated structure of the $La_{18}Mg_3Co_{28}$. Observed and calculated neutron powder diffraction profiles are shown in fig. 1. The preliminary proposed incomensurated structure which is along the c-axis with a Mg atom inside the tunnel. The maximum entropy method (MEM) was applied to calculate nuclear density of the unit cell. The output of the calculation is shown in Fig 1. The cut-off intensity was set to 0.5 fm. The area of disordered space where Mg atoms could be located is clearly visible. Other atoms don’t show anisotropy behavior.

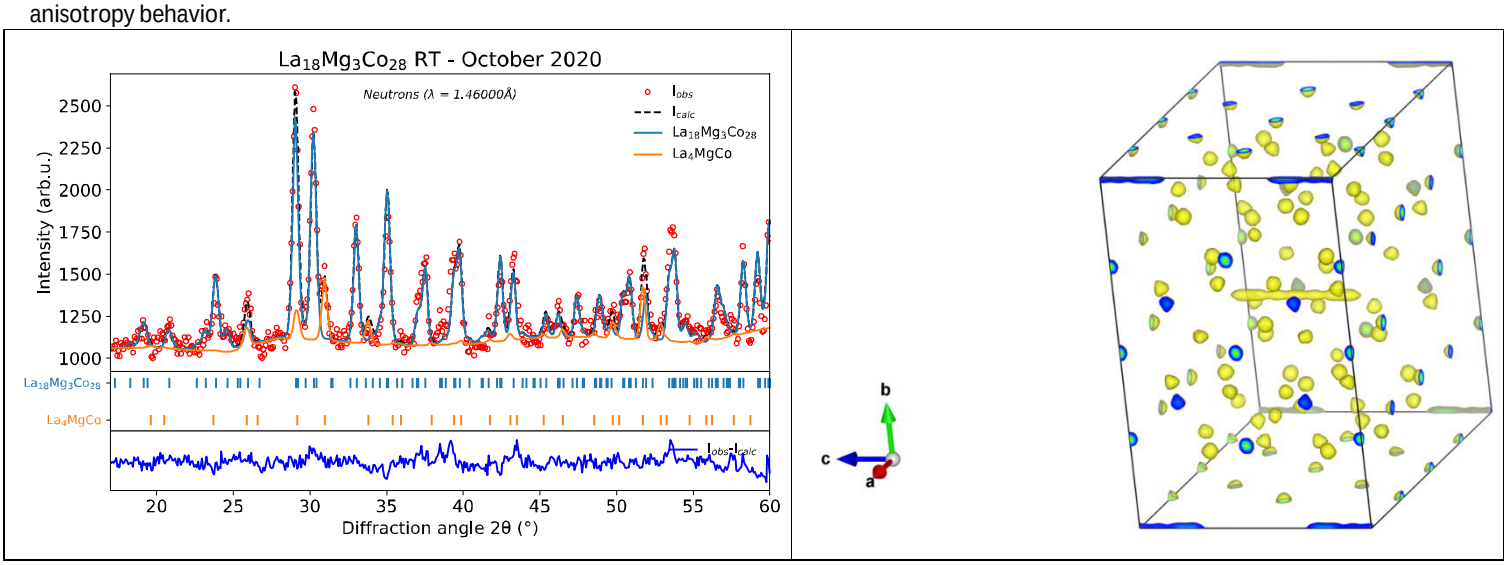

Fig 1. Refinement of the NPD for $La_{18}Mg_3Co_{28}$ at 298K and proposed structure with the nuclear density.

Microstructuring and characterization of hybrid material by Ion micro beam and laser

Laboratory of Tandetron

Mariapompea Cutroneo

Proposal ID

472

Report 472

Microstructuring and characterization of hybrid material by Ion micro beam and laser

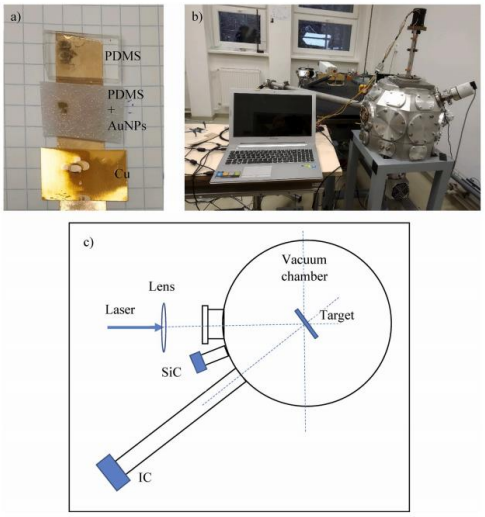

Fig. 1. The picture of the (a) transparent PDMS foil, the opaque PDMS with AuNPs foil and the Cu target (used as reference sample); (b) the laboratory experimental apparatus; (c) scheme of the used experimental set-up.

The investigations of the irradiation of the Q-Switching laser system available at Tandetron lab on PDMS transparent and opaque foils have given interesting information about the generated non-equilibrium plasma, in terms of temperature and density, maximum velocity and energy of the accelerated ions and angular emission of particles.

The shown measurements have permitted to evidence that the used laser, also at high intensity, is very little absorbed in the pristine transparent PDMS, thus acting like a flexible glass. Therefore, this material appears as strategic because it is not damaged by a single laser pulse at intensity of about 10^{10} W/cm^2, unlike many other materials which instead absorb it considerably. Multi pulsed irradiation must be used to produce laser ablation in pure PDMS. The increment of the absorbance in PDMS can be obtained, for example, using AuNPs embedded inside the matrix and generating micrometric pores. This new polymer reduces the laser penetration depth and increases the absorbance so that a plasma and an ablation crater can be produced by a single laser shot. The laser irradiation of PDMS modify the sample composition increasing the carbon and silicon concentration and maintaining the same oxygen amount, as demonstrated by RBS analysis. Enhances the optical absorbance in the near UV and visible region, especially in presence of AuNPs, as UV–visible spectroscopy has confirmed. The Si aggregation and crystallization, especially in presence of the light absorbent AuNPs, was demonstrated by Raman spectroscopy. The modification of the CH3 groups in Si–CH3 structure, whose yield slightly decreases after the laser irradiation in the case of the transparent and virgin PDMS but significantly in the opaque and AuNPs containing PDMS, was demonstrated by µATR-FTIR spectroscopy. The Si nucleation and crystallization are detectable not only in atomic scale, but it is visible also in the micrometric scale by the optical microscope images of the laser irradiated samples indicating presence of crystals of the order of 50–100 µm. By increasing the laser irradiation fluence, the laser irradiated material changes its composition, optical properties, morphology and micrometric structure. In particular, the transparent material becomes opaque and absorbent, the surface irregular and porous, showing a formation of microcrystalline silicon aggregates with a size of the order of 10–90 µm. The increment of the deposited energy in the polymer, in fact, produces molecular scissions and desorption in vacuum, with final enrichment of carbon and silicon concentration and reduction of CH3 groups, with significant enhancement of the laser absorption in the sample. In presence of AuNPs the absorbance is especially enhanced in the wavelength range of 350–600 nm. The laser fluence enhancement increases the ablation yield in vacuum causing more material to be emitted in a vacuum and creating a deeper crater. In addition, the produced plasma enhances in temperature and further changes the material left on the sample in the form of an eroded crater, both laterally and in depth, due to the higher deposited energy, higher temperature and thermal conductivity of the modified composition enriched in carbon and silicon. Preliminary measurements indicating that the laser irradiation in air of the opaque PDMS also produce ablation and surface modification of the polymer composition, which are different with respect to that obtained in high vacuum, however the obtained results have not yet been analysed.

Macroporous PDMS decorated with organic and inorganic materials for application in microelectronics

Laboratory of Tandetron

Mariapompea Cutroneo

Proposal ID

473

Report

A hybrid material incorporating gold nanoparticles (Au-NPs) in polydimethylsiloxane (PDMS) has been synthesized. Gold nanoparticles gained wide interest for their optical, chemical and physical properties, such as surface plasmon oscillations resonant absorption, chemical structure, imaging and sensing. Au-NPs can be conjugated with several functionalizing agents, such as polymeric chains, improving their properties and performances. PDMS composites with weight percentages ranging between 0.1 and 0.2% of spherical Au-NPs (10 nm diameter), were produced. The surface morphology was investigated by atomic force microscopy (AFM) and wetting ability analyses see **Figure 2**.

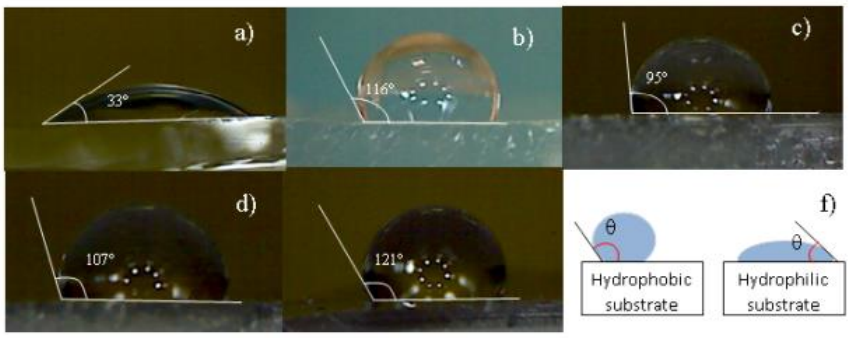

Figure 2. *Optical images for wettability measurements of virgin Glass (a), virgin PDMS (b), PDMS containing 0.1% wt NPs (c) PDMS containing 0.2% wt wet Au-NPs (d) PDMS containing 0.2% wt dried Au-NPs (e) and schematic representation of water molecules on different substrates (d).*

The presence of structures inside both virgin and hybrid PDMS containing Au-NPs was preliminary investigated by Small Angle X-ray Scattering (SAXS). The optical performance of such hybrid material was studied by UV-VIS spectroscopy, in transmission mode.

Polymers containing metal nanoparticles have gained high interest in the optical field, due to their special optical properties, such as dichroism, switching and controlled absorption coefficient. The optical responses of Au-NPs embedded in PDMS films are connected to the Au-NPs features, which result from the adopted method. The PDMS network, does not protect the gold nanoparticles from aggregation as observed in the present study. The changes in the morphological and optical properties of the matrix are related to the presence of the Au-NPs dopants in PDMS working as links uniformly distributed in the polymer. The appearance of pink and violet PDMS-AuNPs composites suggests the presence of Au-NPs aggregates with different size, as confirmed by SAXS and AFM analyses and optical microscopy.

The UV-Vis measurement shows the maximum peak absorption at around 517 nm–528 nm indicating Au-NPs with size ranging between 10 nm and 60 nm in the investigated samples.

The sample exhibiting higher absorption is the PDMS containing 0.2 wt% of Au-NPs due to less aggregation of the fillers and consequent higher number of NPs per volume of matrix. The presence of Au NPs in PDMS improves the absorbance of the matrix as observed also during the laser irradiation of the sample leading to the enhancement of the emitted ion energy, electron density and plasma temperature. It is established that the higher the size of Au NPs is the higher the temperature in the surrounding area and the longer the time to reach the thermal equilibrium. Work is in progress to investigate the thermal behaviour of the PDMS containing Au-NPs, which is crucial for the control of the temperature distribution for applications in metallic micro- and nano-fabrication process by direct laser writing and ion beam writing but also for material growth, material absorption control, cancer treatment and controlled drug release.

Publications:

[1] Cutroneo M.; Havranek V.; Mackova A.; Malinsky P.; Silipigni L.; Slepicka P.; Fajstavr D.; Torrisi L., Synthesis of porous polydimethylsiloxane gold nanoparticles composites by a single step laser ablation process, International Journal of Molecular Sciences 2021

[2] Cutroneo, M.; Havránek, V.; Semián, V.; Torrisi, A.; Macková, A.; Malinský, P.; Silipigni, L.; Slepička, P.; Fajstavr, D.; Torrisi, L. (2021) Porous polydimethylsiloxane filled with graphene-based material for biomedicine. Journal of Porous Materials. 28, 1481-1491.

[3] Cutroneo, M.; Havránek, V.; Macková, A.; Malinský, P.; Torrisi, A.; Silipigni, L.; Slepička, P.; Fajstavr, D.; Torrisi, L. (2021) The characterisation of polydimethylsiloxane containing gold nanoparticles as a function of curing time. Surface and Interface Analysis. 53(7), 618-626. doi: 10.1002/sia.6948

[4] Cutroneo, M.; Havránek, V.; Torrisi, A.; Macková, A.; Malinský, P.; Slepička, P.; Sofer, Z.; Torrisi, L. (2020) Polydimethylsiloxane-graphene oxide composite improving performance by ion beam irradiation. *Surface and Interface Analysis. 52*(12), 1156-1162. doi: 10.1002/sia.6882

Ion beam microstructuring of polymers and carbon allotropes.

Laboratory of Tandetron

Petr Malinsky

Proposal ID

475

Report regarding proposal “Ion beam microstructuring of polymers and carbon allotropes. ”

P. Malinský, A. Macková. K. Szökölová, J. Luxa, P. Slepička, V. Švorčík, Z. Sofer

The proposal was denoted to the study of ion micro-beam irradiation of graphene oxide (GO), polymethylmethacrylate (PMMA) and polyimide (PI) foils with the aim of their reducing and change electrical properties.

Graphene and graphene-like materials have aroused significant interest for supercapacitors and ultra-sensitive gas and liquid detectors because of their remarkably high carrier mobility, extraordinary surface area, 2D structure and cost-effective easy-to-prepare nanoscale morphologies [1, 2]. The cross-linked PMMA and related compounds, Pis and cellulose derivatives have been tested as sensing polymers and non-ionic polar PIs are the most commonly used group of materials for capacitive humidity sensors [3, 4]. The GO, PI and PMMA can absorb liquids or gases that occupy the free space between the polymeric and GO molecules and change its dielectric constant [5].

In our work, the GO, PMMA and PI foils were irradiated using an optimised 5 MeV C^{3+} ion beam with micrometer-scale resolution to induce the carbonisation/deoxygenation/dehydrogenation of the selected area and to enhance the local electrical conductivity. The ion fluence of 1800, 2700 and 3600 nC/mm^2 was used, for which a significant increase of electrical conductivity in GO, PI and PMMA had been reported earlier [6,7]. The irradiated samples were subsequently analyzed by ERDA, RBS, XPS, SEM and Raman spectroscopy to characterize the elemental composition, elemental depth profiles, subsurface chemical bonds and chemical composition modification as well as the surface morphology. The electrical and the sensory properties were tested in environmental chamber with varying humidity and compared with real ceramic capacitors and BME280 combined humidity sensor.

The ion irradiation in GO leads to removal of oxygen functional species and GO reduction accompanied with carbonization of irradiated parts and creation of new carbon bonds. Molecular chain scission, bond cleavages, dehydrogenation and creation of unsaturated bonds together with significant surface destruction is observed in PMMA as a result of the ion irradiation. The ion irradiation of PI leads to the oxidation of very thin surface layer, and to deoxygenation and carbonization in the deeper substrate layers. All these compositional and structural changes in irradiated parts of GO, PMMA and PI samples result in a change of electric conductivity. So that, the irradiated and well organized parts of insulators play the role of capacitor electrodes and non-irradiated parts play the work as an embedded dielectric. These prepared structures were used as capacitors and capacitive/resistive humidity sensors.

The micro-structure with the highest measured capacitance of about 4 pF was prepared on the GO surface. Unfortunately, the capacitance of the micro-structures prepared on the GO surface is evidently influenced by non-negligible conductivity of partially reduced GO between electrodes prepared by ion beam writing. The similar micro-structures prepared on the surface of PI and PMMA exhibit lower capacitance compare to the GO based one. In comparison with GO the PI exhibits much higher radiation resistance. The GO capacity change with change of humidity in atmospheric chamber. On the other side, the polymer components don’t show capacity change with varying humidity but resistance of polymer structures decrease significantly with water vapor concentration in air. In general, we show that the carbon ion micro-lithography is a simple, rapid and green method for fabrication of analog electronic micro-device fabrication need for masks, templates or post-processing.

[1] D. Zhang, et all., Sensor Actuat B-Chem 203 (2014) 263-270.
[2] A. Lamberti, et all., Nanotechnology 28 (2017) 174002.
[3] M. Matsuguchi,et all., Electrochemistry 67 (1992) 2.
[4] Ch. Zhi, Sens, et all., Lett 3 (2005) 274-295.
[5] R. Liu, et all., Sci Rep 7 (2017) 9761.
[6] P. Malinský, et all., Phys Stat Sol 256 (2018) 1800409.
[7] P. Malinský, et all., Surf Coatings Tech 342 (2018) 220–225.

Study of self-assembling effects in plasmonic metal-fullerene mixture films

Laboratory of Tandetron

Vasyl Lavrentiev

Proposal ID

476

Study of self-assembly effects in plasmonic metal-fullerene mixture films

Vasily Lavrentiev

Nuclear Physics Institute AS CR, Rez-130, Husinec 250 68, Czech Republic

In this study, I focused on identification of correlations between metal concentration, x, and surface nanostructure in the self-assembled Au_xC_{60}, Ag_xC_{60} and Cu_xC_{60} nanocomposite (NC) systems fabricated by simultaneous deposition of metal (Au, Ag or Cu) and C_{60} fullerene from vapour [1]. The main results of the study can be reported as the following. 1). RBS analysis does not show existence of oxygen in the Au_xC_{60} and Ag_xC_{60} NC films at any metal concentration, x. Contrary, significant amount of oxygen has been found in the Cu_xC_{60} films that evidences oxidation of the Cu nanoparticles (NPs) formed in the NC films during deposition (see the RBS spectra in Fig. 1). The oxygen concentration, y, gradually increases with x in the $Cu_xO_yC_{60}$ films reflecting growing NP surface fraction (see Fig. 1). 2). AFM study revealed a granular-like structure of the NC film surface (see AFM images in Fig. 1). Size of the granules is clearly varied with x suggesting the effect of metal-C_{60} chemical coupling. Thus, the increase of x in rather dilute films (approximately, with $x<1$) results in some decrease of the granule size. 3). The increase of x also causes non-monotonic variation of the film surface roughness (SR). In the dilute films of Au_xC_{60} and Ag_xC_{60} (with $x<1$), the increase of x results in jump of SR at some critical value of $x=x_{c1}$ ($x_{c1}\approx 1\div 2$, see Fig.1 and [1]) that is caused by formation of enlarged NPs on the film surface. Farther increase of x results in significant surface smoothing and decrease of SR (see Fig.1, in the right). Above $x \approx 15 \div 20$, SR rapidly increases in these films. The variations of SR with x indicate nucleation and growth of the metal NPs in the hybrid films [1]. 4). Interestingly, the increase of x at lower x ($x<1$) in the $Cu_x(O_y)C_{60}$ films results in rapid decrease of SR (see Fig. 1). At higher x ($x>1$), SR gradually increases in these films. Considering RBS results, one can relate such a SR behaviour with oxidation of the Cu NPs growing with x in the NC films. The obtained results will be published in relevant international journals. Some results are reported already in the references listed below.

References.

1. V. Lavrentiev, M. Motylenko, M. Barchuk, C. Schimpf, I. Lavrentieva, J. Pokorny, C. Röder, J. Vacik, A. Dejneka, D. Rafaja. Structure Assembly Regularities in Vapour-Deposited Gold–Fullerene Mixture Films, *Nanoscale Adv*. 2020, **2**, 1542-1550.
2. V. Lavrentiev, D. Chvostova, J. Pokorny, I. Lavrentieva, J. Vacik and A. Dejneka, Interplay of plasmonic and molecule excitations in self-assembled silver-fullerene nanocomposites, *Nanoscale* 2021 (submitted).

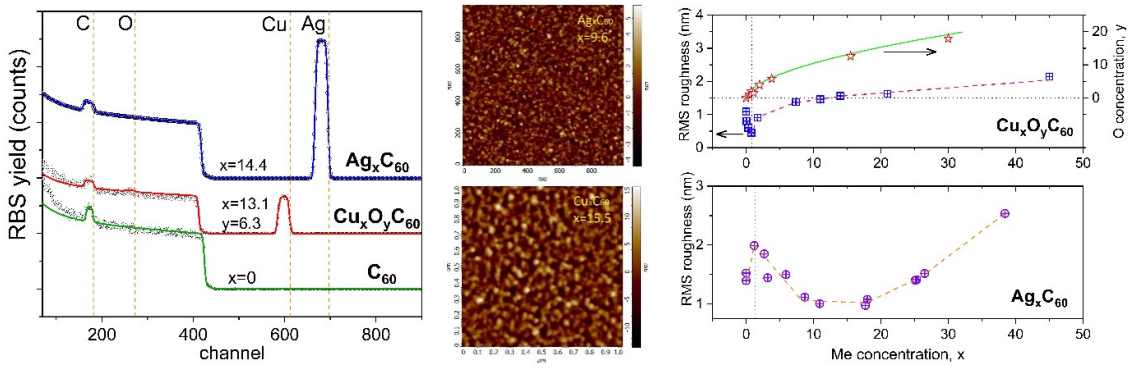

Figure 1: (*in the left*) Typical RBS spectra of the self-assembled Ag_xC_{60} and Cu_xC_{60} films shown for specific metal concentrations, x. RBS spectrum of pure C_{60} film ($x=0$) is also presented for comparison. Experimental and simulated spectra are shown by open dots and coloured curves, respectively. Vertical dotted lines indicate spectral position of the relevant elements located at the sample surface. (*in the middle*) Typical AFM images of Ag_xC_{60} (upper image) and Cu_xC_{60} films (lower image). (*in the right*) SR of the film surface as function of x shown for Cu_xC_{60} films (upper frame) and for Ag_xC_{60} films (lower frame). The upper frame also demonstrates dependence of oxygen concentration on x that is essential for Cu_xC_{60} films (stars, green curve).

Ion channelling effect and damage accumulation in yttria-stabilized zirconia implanted with Ag ions

Laboratory of Tandetron

Romana Mikšová

Proposal ID

477

Report regarding proposal "Ion channelling effect and damage accumulation in yttria-stabilized zirconia implanted with Ag ions."

R. Mikšová, A. Macková, A. Jagerová, P. Malinský, Nuclear Physics Institute of the CAS, v. v. i., Řež, Czech Republic
P. Harcuba, J. Veselý, Department of Physics of Materials, Faculty of Mathematics and Physics, Charles University, Czech Republic
V. Holý, Department of Condensed Matter Physics, Faculty of Mathematics and Physics, Charles University, Czech Republic
CEITEC at Masaryk University, Brno, Czech Republic
Institute of Ion Beam Physics and Materials Research, Helmholtz Zentrum Dresden-Rossendorf, 01328, Dresden, Germany

YSZ crystals were implanted with 400-keV Ag^+ ions over a broad fluence range at RT in three main crystallographic directions (100, 110, 111). This work aimed to investigate the relationship between the surface crystallographic orientation and the subsurface damage induced by Ag^+-ion implantation.

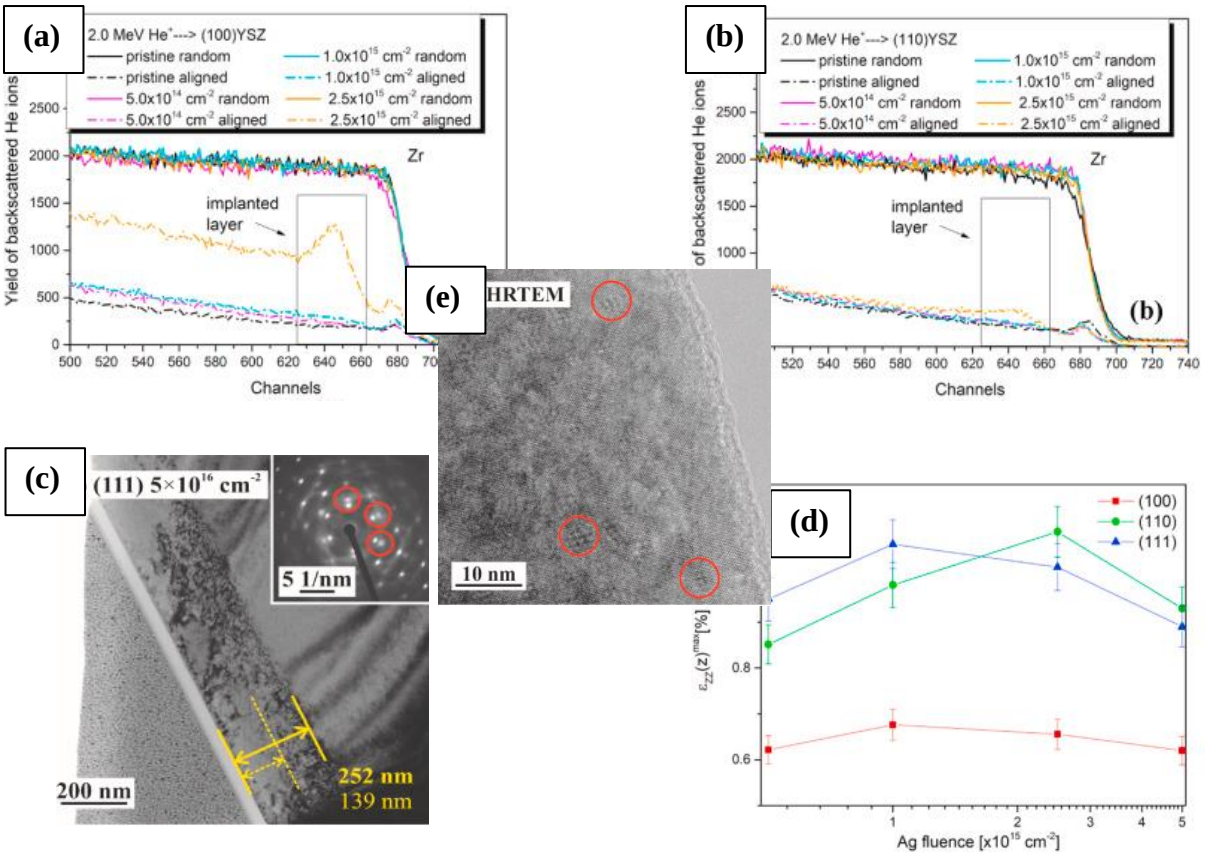

The full amorphisation of YSZ may not be possible under 400-keV Ag^+ irradiation at the ion fluences from 5×10^{14} to 5×10^{16} cm^{-2} at RT irrespective of crystallographic orientation. RBS-C measurements have revealed that the crystalline lattice of YSZ has been damaged but remains crystalline, which has been confirmed by TEM. RBS-C has shown that (110)-oriented YSZ is more radiation-tolerant than (100)- and (111)-oriented YSZ and the damage level f_{max} is below 0.3 (see Figure (a) and (b)).The damaged layer expands deeper in (110)-oriented YSZ than in the other two YSZ orientations; at the fluence of 5×10^{16} cm^{-2}, however, we already observed significant deepening of the damaged layer, comparable in all YSZ orientations (Figure (c)). XRD has characterised the structural damage in a broad range of fluences, where the tensile strain first increased and then relaxed (Figure (d)). The formation of Ag NPs is independent of the crystallographic orientations, which has been shown in TEM, and it is observed for the highest Ag-ion fluence used in the experiments (Figure (e)).

The results were published in NIMB a VACUUM.

Self-assembled stimuli-responsive polymersomes loaded with doxorubicin for tumor drug delivery

Neutron Physics Laboratory - Neutron diffraction

Petr Stepanek

Proposal ID

478

Report regarding proposal Self-assembled stimuli-responsive polymersomes loaded with doxorubicin for tumor drug delivery

P. Štěpánek, A. Jager, Institute of Macromolecular Chemistry CAS, Prague, Czech Republic.

The main aim of this proposal was to determine the influence of the pH on doxorubicin (DOX) partition between the aqueous phase and the hydrophobic membrane of the vesicle during the polymersomes preparation by microfluidic nanoprecipiation which is of fundamental importance on the control of the DOX loading process into polymersomes. Preliminary measurements by dynamic light scattering have shown that the average size of the polymersomes exceeds 100 nm in diameter. Several samples were investigated on the spectrometer MAUD varying in composition and concentration of the polymer and in the drug loaded contents, as described in the proposal. For the majority of the investigates samples the scattered intensity of the neutron beam was very low. Nevertheless, one sample No. 35 yielded sufficient intensity that made it possible to combine the scattering curve with data obtained on the sample sample at ILL in Grenoble (Fig. 1)

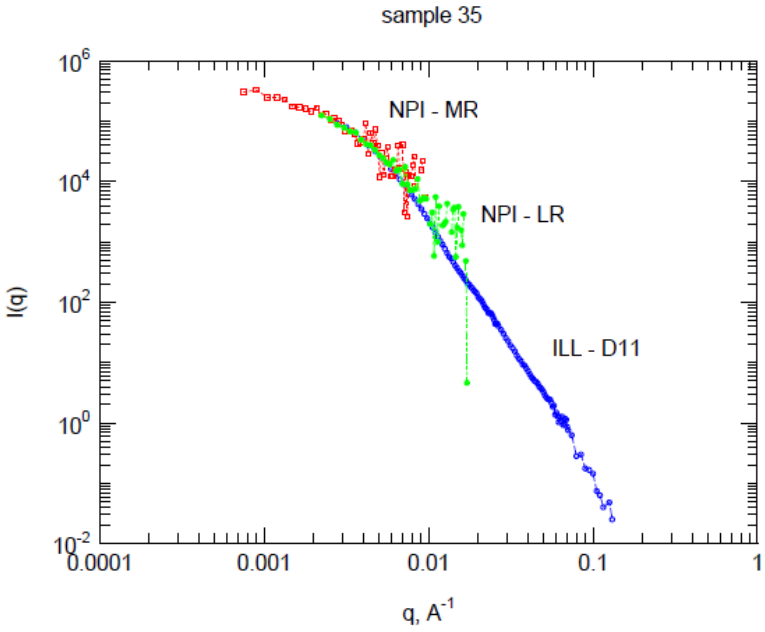

Figure 1. Superposition of scattering curves obtained at NPI-MAUD and at ILL-D11 for a sample 35 of polymeric polymersomes at room temperature.

The data are still under evaluation, but it was already established that for sufficiently scattering polymersome samples the data obtained at NPI are essential for determining the large-scale properties od the polymersomes and will facilitate the analysis of data obtained at D11 at ILL that lack the low-q range.

Lattice parameters and internal stresses determination in the 3D printed steel

Neutron Physics Laboratory - Neutron diffraction

Alena Michalcová

Proposal ID

483

Final report of proposal „Lattice parameters and internal stresses determination in the 3D printed steel"

Seven samples of martensitic steel were studied during the experiment and the results were compared to the Fe etalon. The aim of this study was to explain structure and mechanical properties of prepared materials and materials after subsequent heat treatment.

The first batch of samples was prepared by additive manufacturing processing (also known as 3D printing). The initial powder alloy was gas atomized, which is process also used for rapid solidification. Because of this, the difference in peak position of the powder alloy and the Fe etalon is the most significant. Rapidly solidified powder is formed of supersaturated solid solution of alloying elements in the iron matrix and this fact influences the lattice parameter. On the other hand, the powder alloy can be considered as deformation stress free and the increase of FWHM is probably caused only by presence of fine grains in the material. The curve of additive manufactured sample exhibited smaller difference in the peak position. It can be deduced from this information that the cooling rate during additive manufacturing is slower than the one during gas atomization. The traditional way of steels heat treatment has two steps: 1) solution annealing (at 820 °C with the aim of obtaining supersaturated solid solution of alloying elements in the matrix) and 2) aging (at 490 °C allowing formation of fine precipitates). The mechanical properties of the material with complex heat treatment and the only aged material exhibited comparable values. By the ND techniques was proven that the lattice parameters were also comparable. This result can save the homogenization annealing step of het treatment that is very energy consuming.

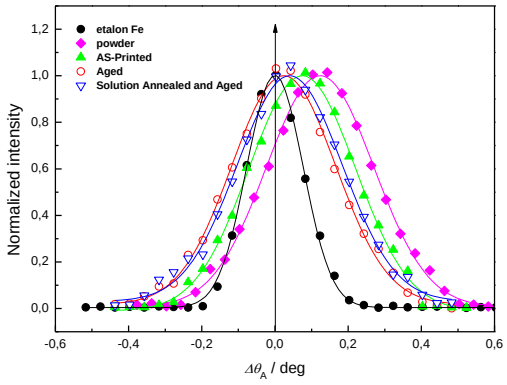

Fig. 1. ND results of additive manufactured materials

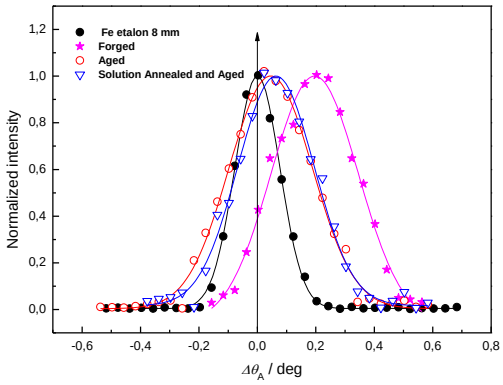

Fig. 2. ND results of forged materials

The other batch of samples was process by rotary swaging that is very intensive technology of forging. The samples were heat treated in the same way as the additive manufactured materials. The results obtained by measuring of the forged materials were comparable to previously shown results, which proved that the energy input of rotary swaging is sufficient to structure distortion and formation of supersaturated solid solution.

Investigation of deformation mechanisms in textured magnesium alloy

Neutron Physics Laboratory - Neutron diffraction

Jan Dittrich

Proposal ID

484

Report regarding proposal "Investigation of deformation mechanisms in textured magnesium alloy"

Due to its hexagonal close-packed lattice the deformation behavior of magnesium and its alloys is rather complex. There are several possible deformation mechanisms – slip systems are basal slip $(0001)\langle 11\bar{2}0\rangle$, prismatic slip $\{10\bar{1}0\}\langle 11\bar{2}0\rangle$ and second order pyramidal slip $\{11\bar{2}2\}\langle 11\bar{2}3\rangle$; other possibility is activation of deformation twinning, namely extension twinning $\{10\bar{1}2\}\langle 10\bar{1}0\rangle$, compression twinning $\{10\bar{1}1\}\langle 10\bar{1}2\rangle$ or double twinning $\{10\bar{1}1\}-\{10\bar{1}2\}$ [1]. In order to meet the Von Mises criterion [2] and achieve homogenous plastic deformation a mechanism providing elongation along the <c> axis, typically the extension twinning or the second order pyramidal slip, needs to be activated. The activation of any given deformation mechanism is strongly dependent on the alloying elements, temperature and the combination of texture and loading direction – the last of which was investigated in this study.

The AZ31 magnesium alloy used in this study exhibited a typical texture of wrought alloys, i. e. basal texture in the normal plane of the sheet (Fig 1). The effect of texture on activity of the individual deformation mechanisms (following the Schmid law [3]) can be examined by deformation of samples machined in various directions with regards to the sheet texture in such way that they are preferentially oriented for different deformation mechanisms. Four orientations were selected – RD (rolling direction), ND (normal direction), 45 (direction at 45° between RD and ND) and 30 (direction at 30° between rolling direction and transversal direction).

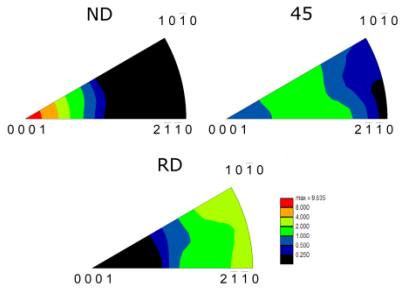

Figure 1 Inverse pole figure (IPF) of the ND, 45 and RD oriented samples.

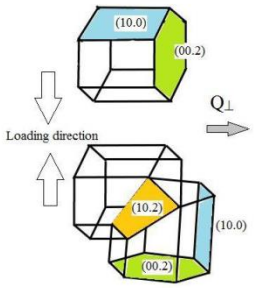

Figure 2 Extension twinning$\{10\bar{1}2\}\langle 10\bar{1}0\rangle$ in compression [4]

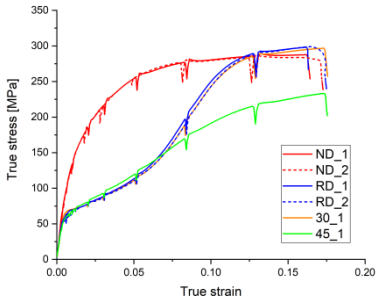

Figure 3 True stress – true strain deformation curves

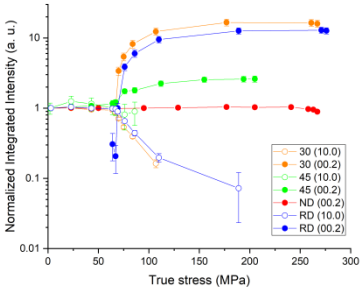

Figure 4 Normalized integrated intensities of the $(10\bar{1}0)$ and (0002) diffraction peak

The extension twinning$\{10\bar{1}2\}\langle 10\bar{1}0\rangle$, being the preferred deformation mechanism for the compressive deformation of the RD and 30 samples, is accompanied by rapid reorientation of the twin by 86,3° with regards to the parent grain (Fig. 2). This is accompanied by shift of diffracted intensity from the $(10\bar{1}0)$ plane to the (0002) plane and can be thus evaluated based on the measured neutron diffraction spectra. A supplementary recording of the acoustic emission signal during loading of the samples provides further and complementary information about the activity of the individual deformation mechanisms.

Neutron diffraction spectra were measured on samples of all above mentioned orientations using the two-axis diffractometer TKSN-400. The samples were strained up to fracture and the experiment was interrupted at 3 points in the elastic part and at selected values of strain in the plastic region (0.5, 1, 2, 3, 5, 8, 12 and 15%) in order to collect the diffraction data (Fig 3).

The $(10\bar{1}0)$ to (0002) peak intensity shift was very significant in the RD and 30 samples, confirming major role of extension twinning particularly in the early stages of plastic deformation. No major differences between these orientations in terms of twinning activity was observed leading to the conclusion that the angle of rotation around the ND direction does not seem to have major influence on mechanical twinning. The 45 sample (oriented favorably for basal slip) also exhibits a certain level of twinning activity, though not as pronounced as the RD and 30 samples. There was no $(10\bar{1}0)$ – (0002) intensity shift observed in the ND sample indicating virtually no extension twinning activity during compressive deformation.

References

[1] Agnew, S. R. and Duygulu, O., 2005, Plastic anisotropy and the role of non-basal slip in magnesium alloy AZ31B, Int. J. Plast., 21 (6), pp 1161-1193
[2] Mises, R. von, 1928, Mechanik der plastichen formänderung von kristallen Zamm – Z., Angew. Math. Me., 8 (3), pp 161-185
[3] Schmid, E. and Boas, W., Plasticity of crystals with special reference to metals, F.A. Hughes, London, 1950.
[4] Máthis, K., Beran, P., Čapek, J. and Lukáš, P., 2012, In-situ neutron diffraction and acoustic emission investigation of twinning activity in magnesium, J. Phys. Conf. Ser., 340

The modification of YSZ implanted with Au using high-energetic oxygen ion irradiation

Laboratory of Tandetron

Romana Mikšová

Proposal ID

486

Report regarding proposal "The modification of YSZ implanted with Au using high-energetic ion irradiation"

Romana Mikšová[1], *Jakub* Cajzl[3], and *Anna* Macková[1,2]
[1]Nuclear Physics Institute of the Czech Academy of Sciences, p.r.i, 250 68 Řež, Czech Republic
[2]Department of Physics, Faculty of Science, J.E. Purkyně University, Pasteurova 3544/1, 400 96 Ústí nad Labem, Czech Republic
[3]Department of Inorganic Chemistry, University of Chemistry and Technology in Prague, 166 28 Prague, Czech Republic

(100)-oriented YSZ crystals were implanted with 1 MeV Au^+ ions at ion fluences of 1.5×10^{16} cm^{-2}, 5.0×10^{16} cm^{-2} and 7.5×10^{16} cm^{-2} and subsequently annealed at 1100 °C in the air for 1 hour. The Si-ion irradiation with energy 10 MeV was used to modify the created Au NPs. The RBS-C spectra (Figure (a) and (b)) showed higher damage in Zr-sublattice up to the projected range of Au ions in YSZ after the ion implantation. Subsequent annealing caused only partial healing of the crystalline YSZ structure, especially in the surface region and two lower ion fluences. 10 MeV Si-ion irradiation increased the disorder in the surface damage region, no additional disorder was observed in the deeper damage region.

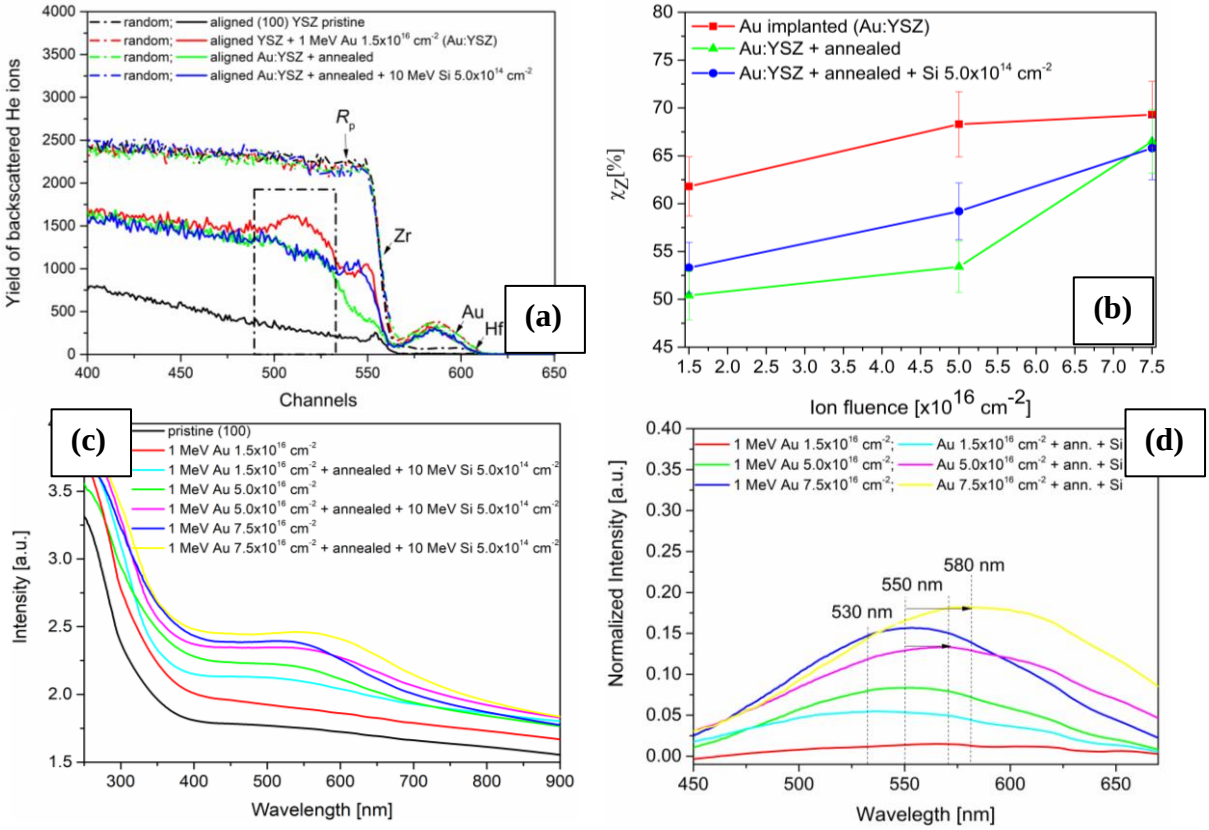

The optical measurement showed the presence of Au NPs. Their growth was more pronounced for the two higher Au-ion fluences, where SPR peaks at 550 nm were shown (Figure (c)). The band was previously connected with two defect types: oxygen vacancies with trapped electrons (F-type centres) nearest to Zr^{4+} cations and hole trapped oxygen ions (V-type centres) adjacent to Y^{3+} cations. After annealing and Si-ion irradiation, the shift of SPR to higher wavelengths (~580 nm) was observed for the two higher ion fluences. It was connected to Au NPs clustering or increasing the size of NPs. For the lowest ion fluence, the SPR peak was observed at ~530 nm (Figure (d) – turquoise line), which correspond to Au NPs formation after annealing.

The part of the results was presented at Applied Nuclear Physics Conference 2021 and published in EPJ proceedings. The next publication will be published in Vacuum in the middle of 2022.

Production of a Co-56 quasipoint source for efficiency calibration of a HPGe detector

Laboratory of Cyclotron and Fast Neutron Generators

Jan Kuera

Proposal ID

230

Report regarding proposal "Production of a ^{56}Co quasipoint source for efficiency calibration of a HPGe detector"

Jan Kučera, Marie Kubešová, Ondřej Lebeda, Nuclear Physics Institute of the Czech Academy of Sciences, Husinec-Řež 130, Czech Republic

A quasi-point ^{56}Co calibration source was prepared by irradiation of a 70 µm thick ^{nat}Fe foil (99.998%) fixed in a target holder of our own design and construction on the external beam line of the cyclotron 120U M. Short irradiation (15 min) with the 14.4 MeV proton beam of 3.2 µA current yielded ^{56}Co activity of 327.8 ± 3.4 kBq (combined uncertainty coverage factor k = 1) as determined by measurement of the 846.8 keV gamma-line. The ^{56}Co source contained only trace activities of ^{57}Co (0.53%) and ^{58}Co (0.26%) relative to ^{56}Co, which did not disturb the use of the ^{56}Co radionuclide for efficiency calibration in the high-energy region. The use of the radionuclide ^{56}Co for calibration of the full energy peak efficiency, ε, of a coaxial HPGe detector, in addition to the commonly employed set of activity standards (^{133}Ba, ^{241}Am, ^{152}Eu, ^{57}Co, ^{137}Cs, ^{88}Y, ^{65}Zn), affected markedly the ε values in the high energy region as demonstrated in Fig. 1. The differences of the ε had a significant impact on the accuracy of Ca determination by k_0-neutron activation analysis with k_0 standardization (k_0-NAA) as demonstrated in Table 1.

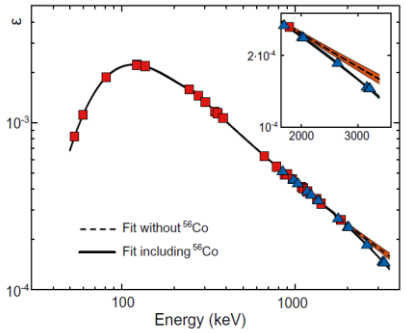

Fig. 1. Full energy peak efficiency of a HPGe detector determined without (squares) and with ^{56}Co (triangles).

Table 1. Results of Ca determination by k_0-NAA in three NIST standard reference materials (SRMs)

Material—ε calibration used	Ca content ± U[a] (%)	$U_{rel.}$ (%)[a]	Ratio[b]
NIST SRM 1547—without ^{56}Co	1.40 ± 0.10	7.1	89.7%
NIST SRM 1547—with ^{56}Co	1.62 ± 0.11	6.8	103.8%
NIST SRM 1547—NIST value	1.56 ± 0.02		–
NIST SRM 1633b—without ^{56}Co	1.31 ± 0.10	7.6	86.8%
NIST SRM 1633b—with ^{56}Co	1.50 ± 0.11	7.3	99.3%
NIST SRM 1633b—NIST value	1.51 ± 0.06		–
NIST SRM 2711—without ^{56}Co	2.52 ± 0.19	7.5	87.5%
NIST SRM 2711—with ^{56}Co	2.78 ± 0.20	7.2	96.5%
NIST SRM 2711—NIST value	2.88 ± 0.08		–

[a]expanded uncertainty (coverage factor $k = 2$)
[b]determined/certified

We demonstrated that the full energy peak efficiency of an HPGe detector in the extended energy range up to ~ 3100 keV is essential for the accurate Ca determination by k_0-NAA. The use of ^{56}Co for the detector efficiency calibration resulted in substantial improvement of the accuracy of Ca determination by k_0-NAA via the ^{49}Ca radionuclide, which emits predominantly 3084.4 keV gamma-rays, as demonstrated by analysis results of NIST SRM 1547 Peach Leaves, NIST SRM 1633b Constituent Elements in Coal Fly Ash, and NIST SRM 2711 Montana II Soil.

References

1. Jan Kučera, Marie Kubešová, Ondřej Lebeda, Improvement of the accuracy of Ca determination with k_0-INAA using an HPGe coaxial detector with extended energy range efficiency calibration, 7th Int. k_0-Users' Workshop, 3-8 September 2017, Montreal, Canada, Book of Abstracts, p. 28.
2. Jan Kučera, Marie Kubešová, Ondřej Lebeda, Improvement of the Ca determination accuracy with k0-INAA using an HPGe coaxial detector with extended energy range efficiency calibration, J. Radioanal. Nucl. Chem. 315 (2018) 671–675.

Study of neutron generation inside target made from lead spheres

Laboratory of Cyclotron and Fast Neutron Generators

Ondej Šastný

Proposal ID

487

Final report for experiment

Study of neutron generation inside target made from lead spheres

Ondřej Šťastný, Brno University of Technology

This experiment was aimed to study spatial and energy distribution of neutrons generated inside target made from small lead spheres. This research was focused on advanced spallation target design. It was planned to perform comparison of experimental data and results of simulations using various codes and libraries.

Unfortunately, due to COVID-19 pandemic and resulting restrictions together with several technological challenges, it was decided to postpone this experiment. Especially, the cooling of target must be considered carefully since the lead spheres would easily melt during irradiation phase.

I would like to express my acknowledgment to the Laboratory of Cyclotron and Fast Neutron Generators' staff, especially to Messrs. Jan Štursa and Václav Zach for their assistance, valuable comments, and cooperation.

Investigation of irradiation induced defects in new materials for nuclear reactors: Zr, Ti based al

Laboratory of Tandetron

Jakub Cizek

Proposal ID

423

Investigation of irradiation induced defects in new materials for nuclear reactors: Zr, Ti based al – Final report

Several alloys consisting of refractory metal elements Hf, Nb, Ta, Ti, Zr have been prepared by arc melt casting. The chemical composition and basic properties of samples studied are summarized in Table 1. The alloys were irradiated with 2.9 MeV protons at room temperature using a Tandetron accelerator. Annealing was performed in several steps with fluence gradually increasing from 10^{15} to 10^{16} cm^{-2}. The samples were investigated after each irradiation step in order to study the development of irradiation-induced defects with increasing fluence.

Table 1 *List of refractory metal alloys studied in the present work. The table shows the composition of each alloy; atom misfit parameter (δ) representing a measure of the magnitude of lattice distortions; configurational entropy of random solid solution (S^{SS}); results of tensile test with constant strain rate of 2×10^{-4} s^{-1}: yield strength (YS), ultimate tensile strength (UTS) and elongation-to-failure (A_{max}); Vickers hardness (HV) measured using load of 0.5 kg applied for 10 s; and the average cross-section for absorption of epithermal neutrons (σ).*

composition	δ (%)	S^{SS} (R)	YS (MPa)	UTS (MPa)	A_{max} (%)	HV (GPa)	σ (barn)
NbTaTi	1.05	1.10	620	683	18.5	2.42 ± 0.02	9.3
NbTaTiZr	4.83	1.39	1144	1205	6.4	3.64 ± 0.02	7.0
$Nb_{0.5}TaTiZr_{1.5}$	5.22	1.32	-	843	0	4.80 ±0.03	6.9
HfNbTaTiZr	4.98	1.61	1155	1212	12.3	3.48 ± 0.03	23.3

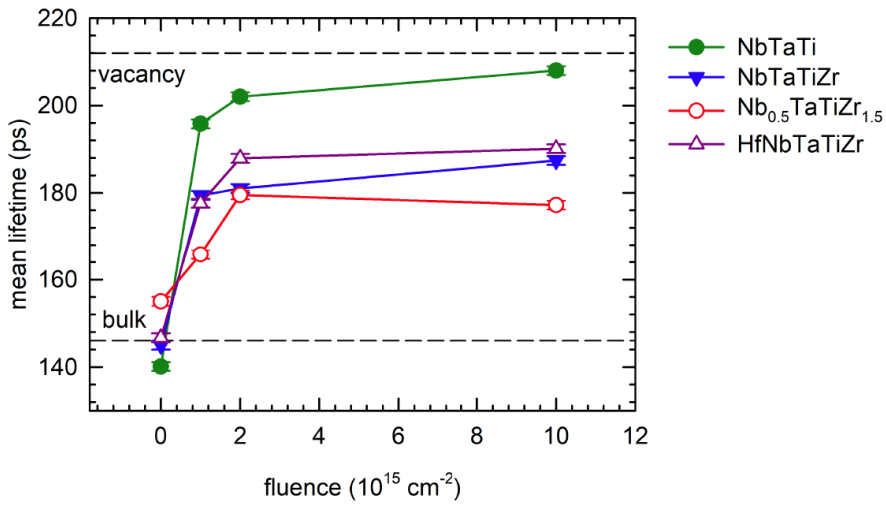

Figure 1 *The development of the mean positron lifetime of NbTaTi, NbTaTiZr, Nb0.5TaTiZr1.5 and HfNbTaTiZr alloy with the irradiation fluence.*

Fig. 1 shows the development of the mean positron lifetime with increasing irradiation fluence. The mean positron lifetime is a robust parameter which is only slightly affected by correlations between the fitting parameters. It is useful for observation of trends occurring during irradiation. The virgin samples exhibit single component LT spectra indicating that positrons are annihilated in single state. Virgin state of the alloys studied is characterized by the lifetime in the range 140-155 ps corresponding to the bulk lifetime, i.e. the lifetime of free positrons not trapped at defects. Hence, the concentration of defects in these alloys is very low and virtually all positrons are annihilated in the free state. Proton irradiation led to an increase of the mean positron lifetime due to formation of radiation-induced defects. The mean lifetime of all alloys increases with increasing fluence indicating that the concentration of irradiation-induced defects increases with increasing fluence. The most pronounced increase of the mean positron lifetime was observed for the NbTaTi alloy. For the highest fluence of 10^{16} cm^{-2} the mean lifetime approaches 210 ps corresponding to lifetime of positrons trapped in monovacancy testifying that majority of positrons is trapped in vacancies. The NbTaTiZr and HfNbTaTiZr alloys exhibit comparable increase of the mean positron lifetime but it is remarkably lower than that for the NbTaTi alloy. The lowest increase of the mean positron lifetime was observed in the $Nb_{0.5}TaTiZr_{1.5}$ alloy where the magnitude of lattice distortions is the highest among the alloys studied as reflected by the highest value of the misfit parameter δ, see Table 1.

Hence, the present investigations of refractory metal alloys irradiated by protons confirmed good radiation resistance of HEAs. It seems that good resistance against radiation damage is common property of 3d transition metal and refractory metal HEAs. Radiation resistance of HEAs is directly related to the effect of lattice distortions representing a typical feature of HEA structure.

Study of the fission process at higher neutron energies

Laboratory of Cyclotron and Fast Neutron Generators

David Hladík

Proposal ID

424

Final report regarding the proposal 'Study of the fission process at higher neutron energies'

Small samples of an ^{238}U were irradiated with quasi-monoenergetic neutrons from the cyclotron U-120M with p+^{7}Li and p+Be converter at several peak neutron energies in the range of 17-33 MeV and delayed neutrons (DN) were measured. BF_3 detectors were chosen for the measurement of time distribution of the DN.

New measurement process was developed and tested during several experiments. The goal was to minimize the effect of saturation of the detectors as well as measure even the shortest decay group below 0.5 s after the end of irradiation. This goal was successfully accomplished.

This result was presented at "Second French-Czech « Barrande » Nuclear Research Workshop" in France.

These results can serve as a proof of concept and the work will continue to acquire better precision. Subsequently, the simulation using General Fission Model (GEF) is in progress for further comparison of acquired data

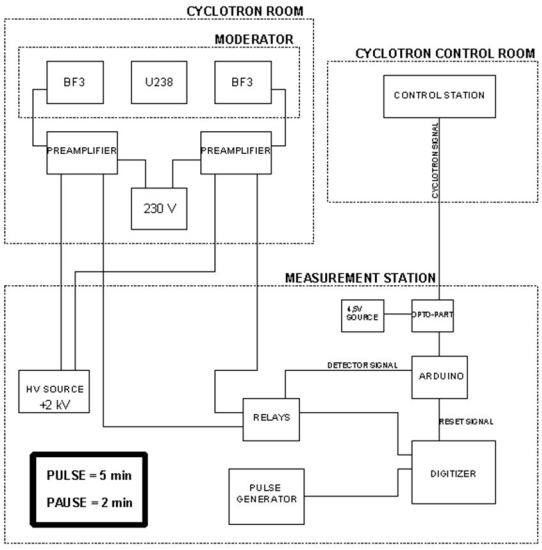

Figure 1. Block scheme of the measurement setting and process

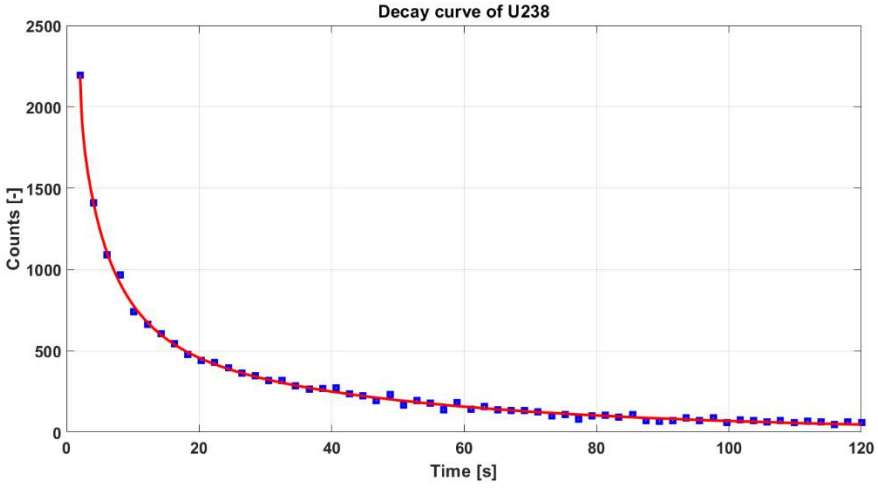

Figure 2. Decay curve obtained from an experiment using p+Be target, En=20 Mev, distance 1 m.

Study of advanced silicon radiation detectors

Laboratory of Tandetron

Maria Marcisovska

Proposal ID

489

Report regarding proposal “Study of advanced silicon radiation detectors”

The conducted experiment was focused on two tasks:

I. Spectral and Angular Response of a Silicon Strip Detector Based on PH32 ASIC
M. Kaschner, P. Stanek, P. Svihra, FNSPE CTU in Prague

The primary focus of the first study is energy calibration of a silicon-strip detector used for alpha particle spectrometry. The energy range of alpha particles used for calibration was from 2 MeV up to 9 MeV. Secondary aim is to observe the effect of the incidence angle on the response of the device. The results will be used for future radionuclide identification and activity measurements.

For the purposes of the study, the detector was placed in a vacuum chamber on a motorized arm, which provides movement of the detector in and out of the particle beam, as well as changes of the angle of the incidence. The measurements required very low particle flux (lower than the minimal detection limit needed by the flux measuring device). In order to reduce the pile-up of the particles in the individual strips, the device was placed outside of the center of the beam which was then collimated to 5×0.2 mm^2. An example of the reproduced spectra is shown in Figure 1a, the dependency of ToT as a function of energy in Figure 1b. The effect of the angle of incidence variation on ToT is in Figure 1c.

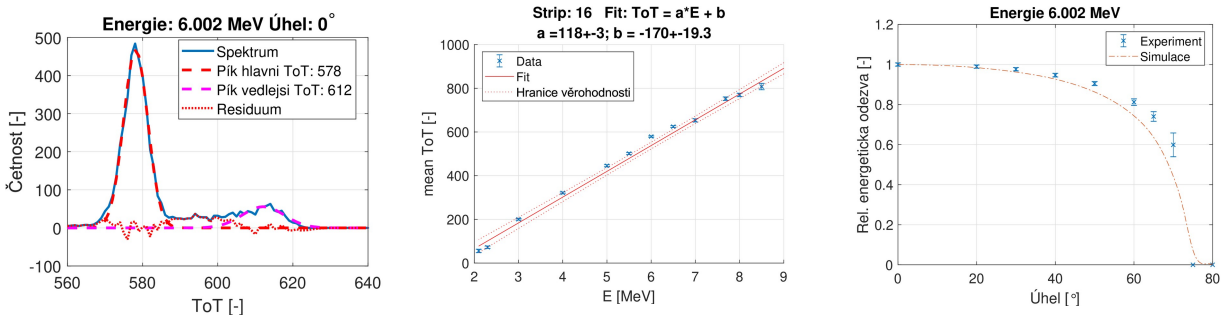

Figure 1: Measured dependencies. (a) Example of measured spectra and locations of visible peaks. (b) Observed dependence of detector response on the energy of alpha particles and its linear fit. (c) Observed dependence of detector response on angle of incidence of alpha particles and expected dependency according to simulations in SRIM.

II. Study of advanced monolithic silicon detectors using highly ionizing ions
M. Havranek, A. Kabatova, A. Kostina, M. Marcisovska, FNSPE CTU in Prague

The second task is aimed at the study of pixel matrix response of the SpacePix and X-CHIP monolithic detectors to different ions.

Protons with an energy of 6 MeV, helium nuclei with an energy of 8-9 MeV and lithium nuclei with an energy of 12 MeV were used for irradiation. The images recorded from the individual sensors were analyzed. Figure 2 shows the interactions of protons, helium nuclei and lithium in the SpacePix-2-Log sensor. The sensor can display individual interactions of all types of ions. Relatively small clusters were observed for all types of ions, rarely exceeding 2×2 pixels in size. Despite the relatively high deposited energies close to the saturation of the measuring channels, a clear difference in the amplitude of the signal from protons and He/Li can be seen. However, to distinguish He from Li, more advanced analysis techniques need to be used, which also take into account the size of the clusters.

The relatively low energy of ions leads to saturation of the sensors. To better understand the response of SpacePix sensors, it is necessary to use ion beams with higher energy in the order of hundreds of MeV, where the ions leave only part of their original energy in the sensitive layer of the sensor and, based on specific energy losses, to test the ability to identify different types of ions.

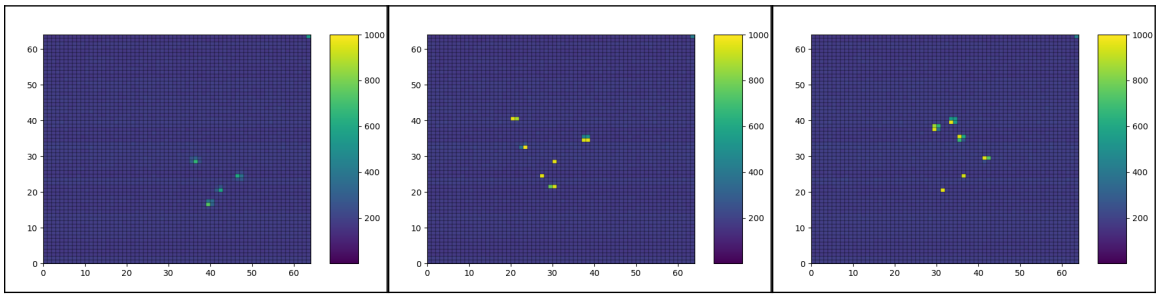

Figure 2: Interactions of protons (left), helium nuclei (middle) and lithium (right) in the SpacePix-2-Log sensor.

Calibration of TimePix detectors and low-energy proton radiography

Laboratory of Tandetron

Václav Olšanský

Proposal ID

426

Report regarding proposal "Calibration of TimePix detector and low-energy proton radiography"

V. Olšanský[1], C. Oancea[2], C. Granja[2], V. Havránek[1], A. Mackova[1], J. Jakůbek[2], Š. Polanský[2], P. Krist[1]

[1] *Nuclear Physics Institute Czech Acad. Sci., Řež, Czech Republic*

[2] *ADVACAM, Prague, Czech Republic*

The goal of these measurements was to perform proton radiography in the air and to characterize the proton and carbon micro-beams in vacuum. Several experimental setups were designed. Firstly, AdvaPix–TimePix3 and MiniPix–TimePix detectors with 300 µm thick Si sensors were calibrated in proton µ-beams and in a wide-area scanning beam. Afterwards, Al and Mylar targets (of various thicknesses from 5 to 30 µm) and more complex target stairs-like (thicknesses of 30, 25, 10, 5 and 0-air) of Al and Mylar, Fig. 1, were used to produce proton radiographies. All targets were placed close to the sensitive Si layer of detector, see Fig.1.

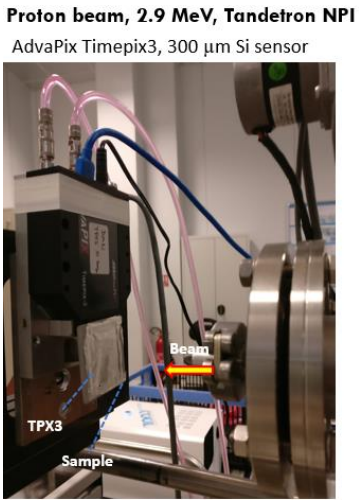

Figure 1 Experimental setup of a proton radiography using Advapix Timepi-3 detector.

The highly integrated signal electronics per-pixel provide fast and dark-current free single particle detection. The hybrid semiconductor pixel detector Timepix-3, Fig. 1, provides high-sensitivity and wide-dynamic range in terms of particle types, fluxes and spectral response. Timepix-3 detector visualizes the track of each individual particle and determines its time of interaction, spatial location and energy loss, see Fig. 2.

This experiment demonstrates the possibility of using low energy protons for radiography of very thin samples. Results have been visualized as images which show one of these distributions: cluster sizes, cluster energy and high. The reconstruction of proton radiography of Al stairs-like target can be seen in Fig. 3. Promising results were obtained based on the cluster area, Fig.3 b), and cluster energy, Fig. 3c). Further investigations of other targets are ongoing.

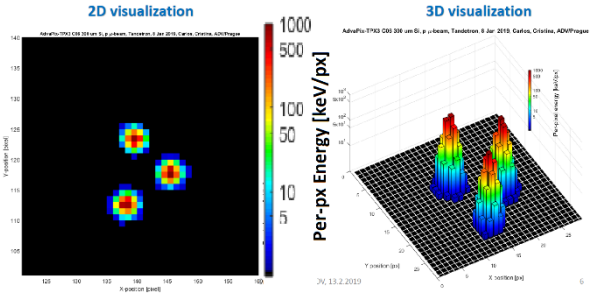

Figure 2 Position- and spectral-sensitive detection of single protons. a) 2D visualization and b) 3D visualization of per-pixel energy (displayed in color scale) of 3 events delivered in spot scanning beam mode [1].

<u>Vacuum measurements using ^{12}C scanning beams</u>

A Minipix Timepix detector was placed inside the vacuum chamber and the Time and spatial distribution of 10 MeV ^{12}C beam were studied. In Fig. 4 is sown the Time and spatial pattern of a scanning beam measured for 1 min. Other energies and scanning patterns were studied.

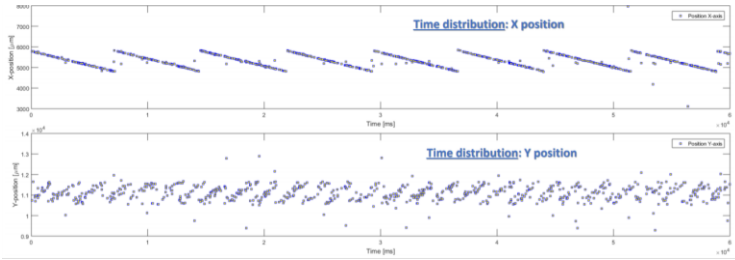

Figure 4 Time and spatial distribution of 10 MeV ^{12}C-ion beams.

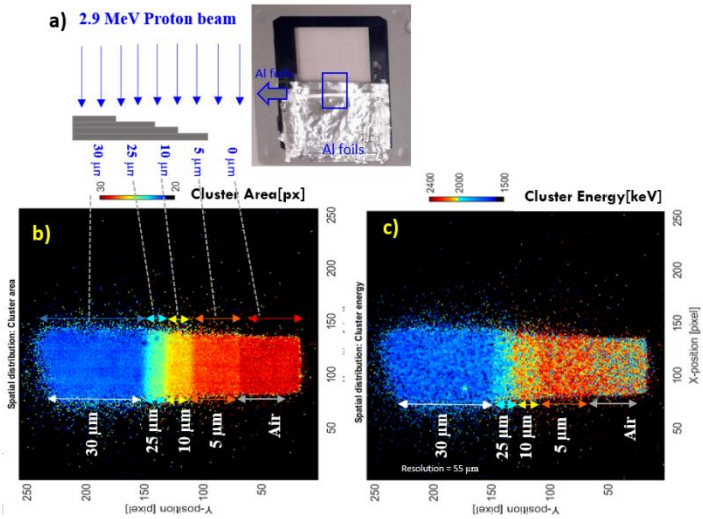

Figure 3 a) Al stair- like target, b) radiography reconstruction of the Al target using cluster area and c) reconstruction using the cluster energy.

Reference: C. Oancea, C. Granja, J. Jakubek, A. Mackova, V. Havranek, V. Olsansky *Charged particle imaging with Timepix a Timepix3 Pixel Detector*, 5th Annual LLU Workshop, USA 2019

Nanostructuring of crystalline ZnO by energetic ion beams for optoelectronic applications

Laboratory of Tandetron

Adela Jagerova

Proposal ID

490

Report regarding proposal "Nanostructuring of crystalline ZnO by energetic ion beams for optoelectronic applications"

Adéla Jagerová[1,2], *Jan* Mistrík[3,4], and *Anna* Macková[1,2]
[1]Nuclear Physics Institute of the Czech Academy of Sciences, p.r.i, 250 68 Řež, Czech Republic
[2]Department of Physics, Faculty of Science, J.E. Purkyně University, Pasteurova 3544/1, 400 96 Ústí nad Labem, Czech Republic
[3]Institute of Applied Physics and Mathematics, Faculty of Chemical Technology, University of Pardubice, 532 10 Pardubice, Czech Republic
[4]Centre of Materials and Nanotechnologies, Faculty of Chemical Technology, University of Pardubice, 530 02 Pardubice, Czech Republic

The surfaces of *c*-, *a*- and *m-plane* ZnO were nano-structured using the 27 MeV W ion irradiation with ion fluences of 5×10^{9}, 5×10^{10} and 5×10^{11} cm^{-2}. RBS-C analysis revealed only low Zn-disorder up to the depth of 1.38 μm in all studied orientations (e.g. Figure 1a for *c-plane* ZnO). The irradiation-induced increase of surface roughness and formation of nano-hillocks on the *c*- and *a-plane* ZnO and huge moulds on the *m-plane* ZnO (Figure 1b and c for *c*- and *m-plane* ZnO, respectively).

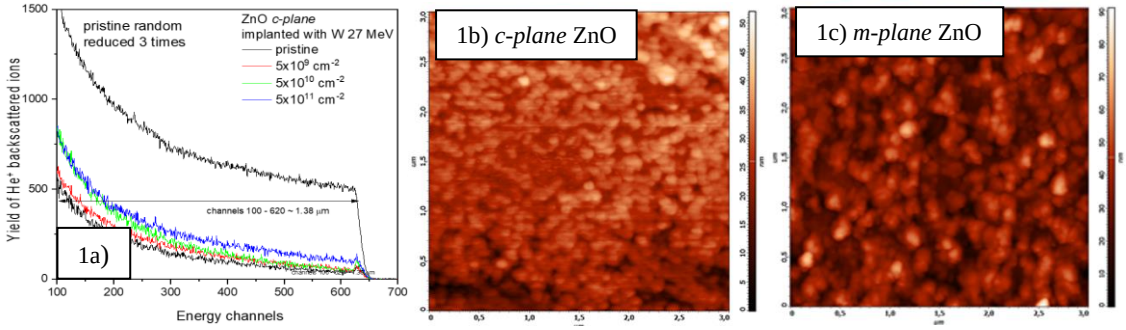

The crystalline ZnO nanopillars with a thickness of about 400 nm were modified with Au NPs prepared by 400 keV Au ion implantation with ion fluences of 1×10^{15}, 5×10^{15} and 1×10^{16} cm^{-2}. The growth of Au NPs was further supported with thermal annealing at 600 °C on air. The ion implantation decreases ZnO nanopillar thickness as observed by RBS (Figure 2a). The implanted Au ions modified the depth of about 250 nm. The higher implantation depth exhibited a shift of implanted Au ions towards the surface, see Figure 2b. The distribution of implanted Au ions did not significantly change after thermal annealing. The optical properties of implanted ZnO nanopillars, expressed by extinction coefficient, showed surfaced plasmon resonance (SPR) peak typical for Au NPs in a wavelength region of 400 – 800 nm, see Figure 2c. The SPR peak is shifted against a higher wavelength with increasing Au ion fluence indicating the creation of bigger Au NPs with higher fluence. SPR peak is further shifted towards a higher wavelength after thermal annealing due to the growth of Au NPs and the formation of bigger complex clusters.

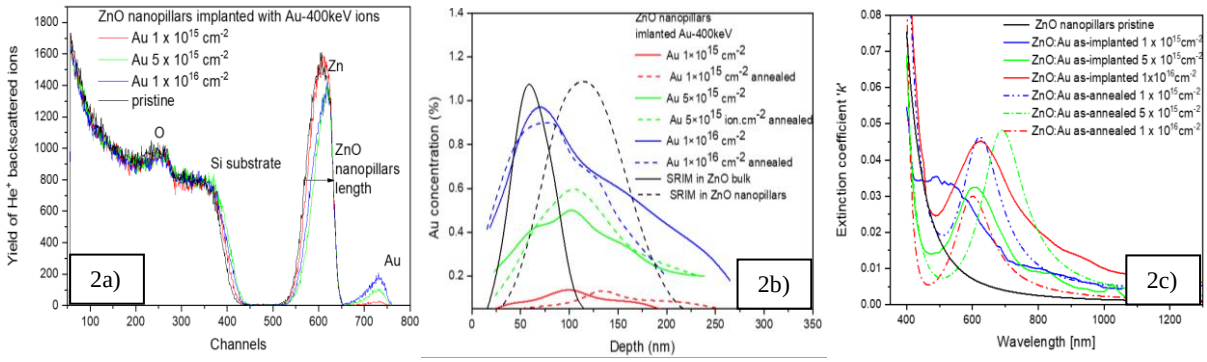

The results obtained for 27 MeV W irradiated *c*-, *a*- and *m-plane* ZnO surfaces were summarized and published in Physical Chemistry Chemical Physics journal. The modification of ZnO nanopillars with Au NPs prepared with 400 keV Au implantation was published in the Journal of Physics D: Applied Physics.

Multielemental analysis of nutrients and pollutants in cultivated O. glaberrima and Sativa rices on

Neutron Physics Laboratory - Nuclear analytical methods with neutrons

Alassane Alassane

Proposal ID

428

Multi-elemental analysis of roots and leaves from Oryza glaberrima rice plants at vegetative stage of growth by combined PIGE, RBS, PIXE and GC-TDS methods

S. Fernandes[a,*], A. Traoré[b], O. Fleury[b], V. Havránek[a], J. Kučera[a], A. Ndao[b]
[a]Nuclear Physics Institute CAS, v.v.i., 250 68, Husinec - Řež, Czech Republic
[b]Institute for Applied Nuclear Technology, Cheikh Anta Diop University, Dakar, Senegal

This study aims at understanding the bioaccumulation and transport mechanisms of both micro- and macronutrients in the leaves and roots of African rice *Oryza glaberrima* Steud (OG) plants cultivated in Senegal during the wet season at the vegetative stage of growth to determine the translocation factors from roots to leaves and to evaluate the suitability of OG rice plants for phytoremediation. A comparative analysis of the elemental composition of roots and leaves of OG plants, provided information on the bioaccumulation of nutrients necessary for plant growth which can become detrimental if their toxicity level is reached. The elemental analysis of basic nutrients (C, H, O), macronutrients (N, P, K, Ca, Mg and S) and micronutrients (Cl, Fe, Cu, Mn, Ni and Zn) in the OG roots and leaves was made possible by several elemental analytical techniques (PIGE, RBS, PIXE and GC-TDS). All methods were validated by analysis of pure substances and certified reference materials. The high accumulation rate of Cu (5 x), Al (4 x) and Fe (~ 2 x) in the OG rice roots relative to the leaves indicates the existence of low translocation factors for these metals from root to leaves probably due to the existence of plant mechanisms to limit their transport and to preferentially accumulate Si (% mass: 5.2 ± 0.5) in the rice leaves. The high accumulation rates of Mn, Ni, Rb and Cr "heavy" metals in the OG leaves relative to the roots, shows that these can be partially removed from soil through phytoextraction processes by harvesting the shoot tissues.

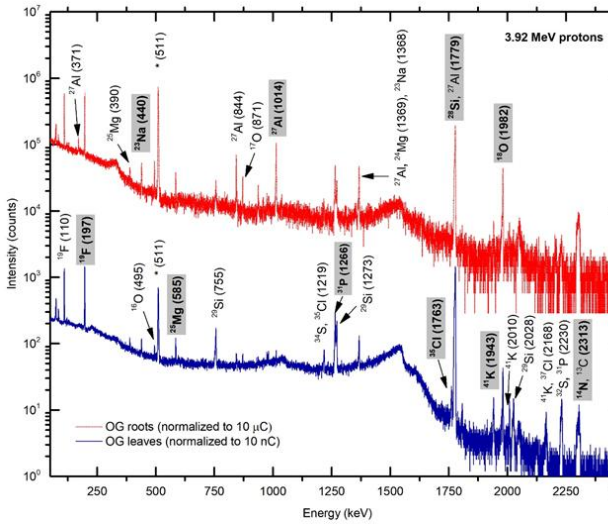

Figure 2 Normalized γ-ray spectrum for OG leaves and roots at 3.92 MeV protons. The γ-energy reference peak used for isotopic quantification is indicated inside grey boxes and highlighted in bold

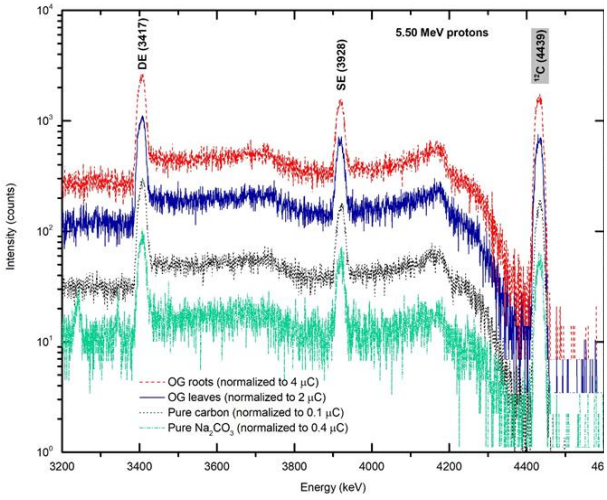

Figure 1 Detail of the normalized γ-ray spectrum of OG leaves and roots, and standard materials C and Na_2CO_3 at 5.5 MeV protons showing the reaction $^{12}C(p,p_1\gamma)^{12}C$ at 4439 keV and its single and double escape peaks.

The determination of the elemental composition of cultivated soil and OG rice stems and grains is necessary to obtain the translocation factors of nutrient and non-nutrient into different plant organs from soil to root and from leaves to grains for characterization of their transport into the plant cells. The analysis of the OG rice grains is needed to testify that all the potential toxic elements identified in this study, and other heavy metals such as As, Sb, Cd, Hg and Pb, known to be absorbed by the plant biomass, were not accumulated to toxic levels for human consumption to ensure food security in West Africa.

[1] S. Bado et al. NIM B 371 (2016) 407 - 412.

Cross-section measurements of the 16O(n,tot) reaction in the neutron energy range 20-35 MeV

Laboratory of Cyclotron and Fast Neutron Generators

Mitja Majerle

Proposal ID

368

Final report regarding proposal 'Cross-section measurements of the ^{16}O(n,tot) reaction in the neutron energy range 20-35 MeV'

The series of transmission experiments with liquid oxygen was performed using Quasi-monoenergetic collimated beams of neutrons produced at U-120M cyclotron. The absolute values of the cross-section ^{nat}O(n,tot) were successfully extracted for four different energies ranging from 18 to 30 MeV. Overall uncertainties were evaluated for each measurement and regarding one sigma interval derived for normal distribution, the precision better than 3 % was achieved.

Exact results were presented at '2019 International Conference on Nuclear Data for Science and Technology' and subsequent paper named 'Total neutron cross-section extracted from transmission experiments with liquid oxygen using neutron energies from 18 to 34 MeV' is about to be published under 'EPJ Web of Conferences' in 2020.

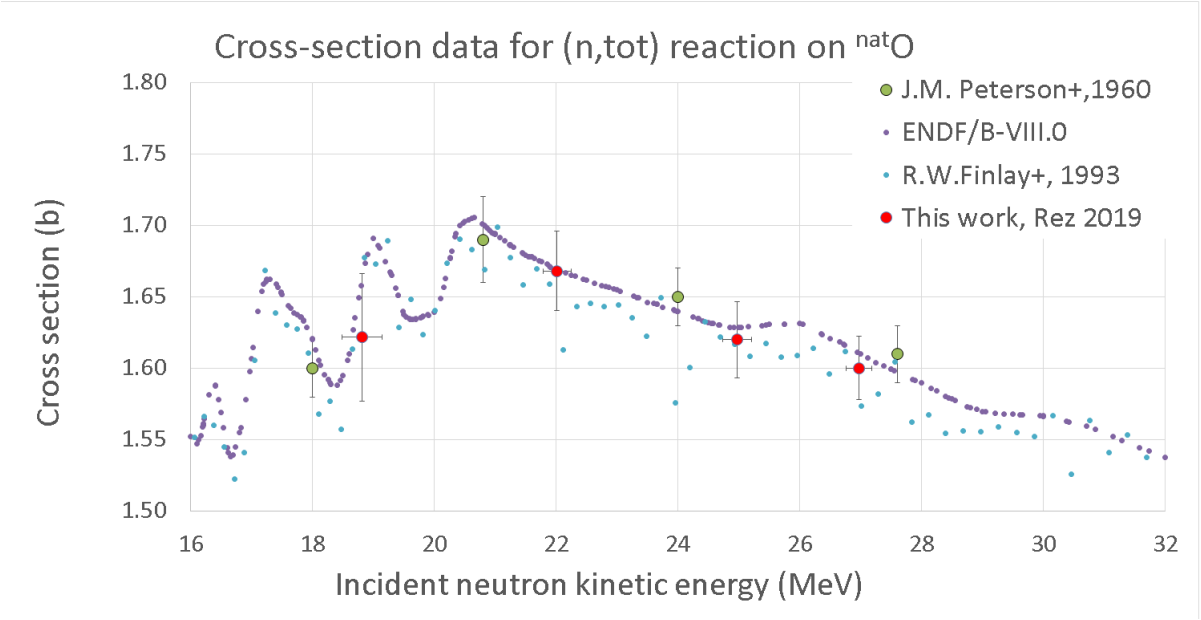

Figure 1. Present data of total neutron cross-section for ^{nat}O are shown (red points). For comparison data of Peterson [1] and Finlay [2] together with ENDF/B-VIII.0 evaluation for 16O(n, tot) reaction [3] are shown.

Present results (figure 1) should improve the correctness of data evaluations and contribute to all projects and researches where cross-section ^{nat}O(n,tot) is not a negligible factor. The Accelerator Driven Systems (ADS) and future fusion-based facilities are relevant examples.

References:

[1] J.M. Peterson, A. Bratenahl, J.P. Stoering, Phys. Rev.120, 521 (1960)

[2] R.W. Finlay et al., Neutron Total Cross Section Measurements at Intermediate Energy, in Nuclear Data for Science and Technology (1992), pp. 720–722, ISBN 978-3-642-58113-7

[3] D. Brown et al., Nuclear Data Sheets 148, 1 (2018), special Issue on Nuclear Reaction Data

Crystal structure studying of the Mn55Al45C2T (T= Mo, Cr, Cu, MoC) alloys

Neutron Physics Laboratory - Neutron diffraction

Vitalii Shtender

Proposal ID

496

Report regarding proposal "Crystal structure studying of the $Mn_{55}Al_{45}C_2T$ (T= Mo, Cr) alloys"

V. Shtender, M. Sahlberg, Uppsala University, Sweden
C. Hervoches P. Beran, Nucl. Physics Inst., Rez, Czech Republic

The goal was to prepare $Mn_{55}Al_{45}C_2$ with well dispersed nanoparticles or carbide former to create pinning sites. For this, we therefore intentionally added different amount of carbides, nitrides and oxides or simple d-metals to the $Mn_{55}Al_{45}C_2$ to elucidate their effect on the microstructure and magnetic properties. Fig. 1a shows XRD pattern for $Mn_{55}Al_{45}C_2Mo_2$ where some over intensities are observed which could relate to the influence of Mo on the structural feature (preffered orientation has been taken into account). As can be seen in Fig. 1b homogeneous distribution of the Mo in alloy matrix has been distinguished (τ /ε phase ration will be improved with annealing). In this proposal we wanted to investigate $Mn_{55}Al_{45}C_2T$ (T= Mo, Cr, Cu and MoC) alloys and find out influence of the dopants on the τ-phase.

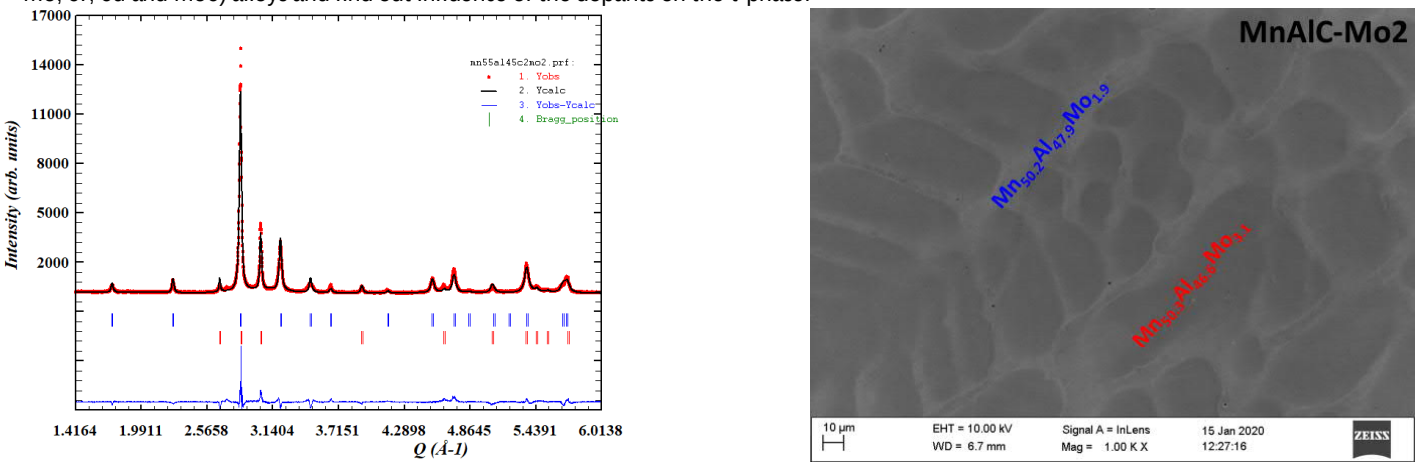

a) *b)*

Figure 1 a) refined XRD of $Mn_{55}Al_{45}C_2Mo_2$ and b) SEM/EDS on the as cast $Mn_{55}Al_{45}C_2Mo_2$ alloy

Neutron powder diffraction experiments were performed on $Mn_{55}Al_{45}C_2Mo_2$ and $Mn_{55}Al_{45}C_2Cr$ at 298 K using the MEREDIT instrument. The motivation for the experiments was to investigate the possible incorporation of the Mo and Cr into the structure of tau-MnAl phase.

The extracted data is still under evaluation but preliminary results propose Mo goes to the structure of tau-phase (the same as it was indicated with SEM/EDS). Observed and calculated neutron powder diffraction profiles are shown in fig. 1. The preliminary proposed magnetic structure which is along the z-axis with a central atom in the opposite direction

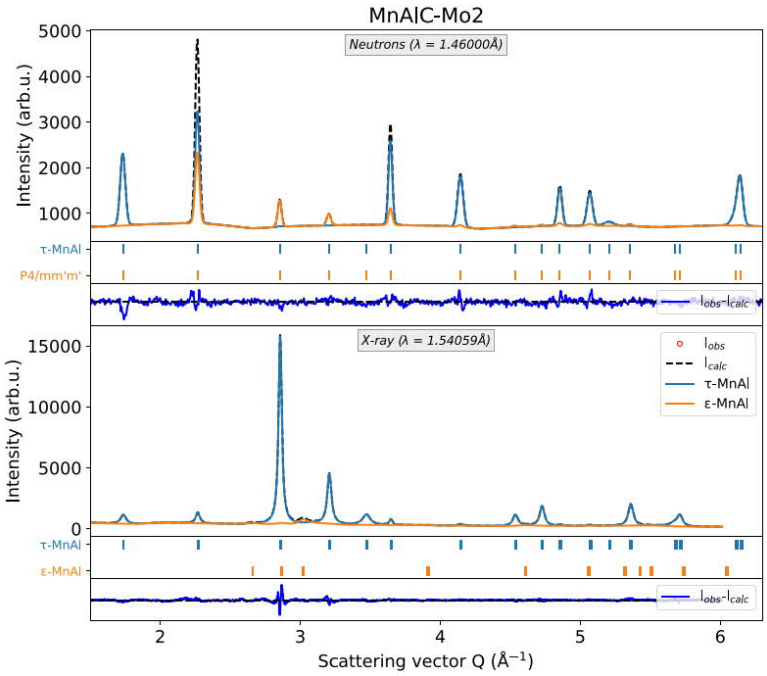

Fig 1. Joint refinement of the XRD and NPD for Mn $Mn_{55}Al_{45}C_2Mo_2$ at 298K.

SINE2020 feasibility study - Determination of bulk residual stress in cold winding springs

Neutron Physics Laboratory - Neutron diffraction

Pavel Strunz

Proposal ID

433

Determination of difference bulk residual strains/stresses profile in cold winding springs and corresponding quenched/tempered wires

In order to fully understand **influence of the bulk residual strains/stresses** developed in steel spring from quenched/tempered ultrahigh strength wire (UTS is around 2000 MPa) after different cold forming/coiling processes followed by various stress relieving annealing **on the safe service life and final mechanical properties** characterized by fatigue strength, it is important to performed non-destructive Strain/Stress analysis by Neutron Diffraction on real Springs.

Two cold-winding springs, denoted “spring A” and “spring B” were scanned at the SPN-100 neutron diffractometer. They correspond to two different technological procedures used for their productions. Rods for d_0 (“stress-free”) determination were measured as well.

A suitable neutron wavelength λ = 2.13 Å and reflection from the examined material [α-Fe (110), lattice spacing a = 2.865 Å] were selected to reach the diffraction angle 2θ near 65°. This is not the geometrically optimum diffraction arrangement. Nevertheless, it ensures low background at the position-sensitive detector and the gauge volume is still of not too much of anisometric shape in this case. The strain (stress) determined in the diffraction experiment was averaged over the gauge volume of 2x2x2 mm^3. In order to determine three stress components, the different geometrical arrangement of the examined specimen with respect to the scattering vector were realized. The necessary configurations are shown in Fig. 1.

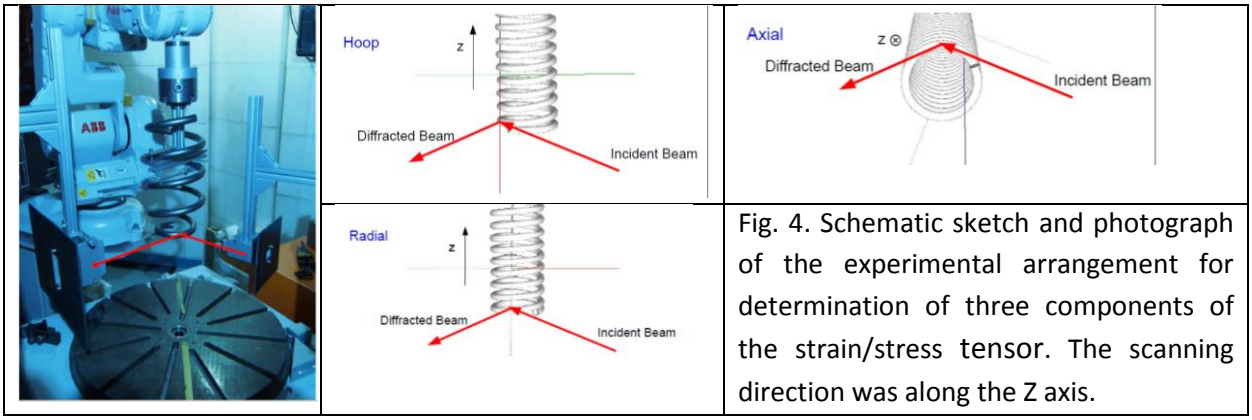

Fig. 4. Schematic sketch and photograph of the experimental arrangement for determination of three components of the strain/stress tensor. The scanning direction was along the Z axis.

The strains measured during through-wire scans are drawn in Fig. 5. For some components of the strain tensor, it was, however, not possible to obtain reasonable results due to attenuation in rather complex shape (spring).

It was found that it is possible to measure residual elastic strains in cold winding springs. The lattice strains were determined along two scans in two different springs. Three points should be, nevertheless, considered for possible further measurements:

1) Other scanning direction should be selected as the gradient of the effect of residual stress should be largest in in-out direction from the spring centre (i.e. not along Z direction).
2) Specimens are of a complex shape. Therefore, some points are hardly measurable in some geometries; consider use of alternative geometry of measurement or stronger neutron source.
3) Notation of direction should be with respect to wire axis, not with respect to spring axis, as these directions are in fact of largest interest for the producer.

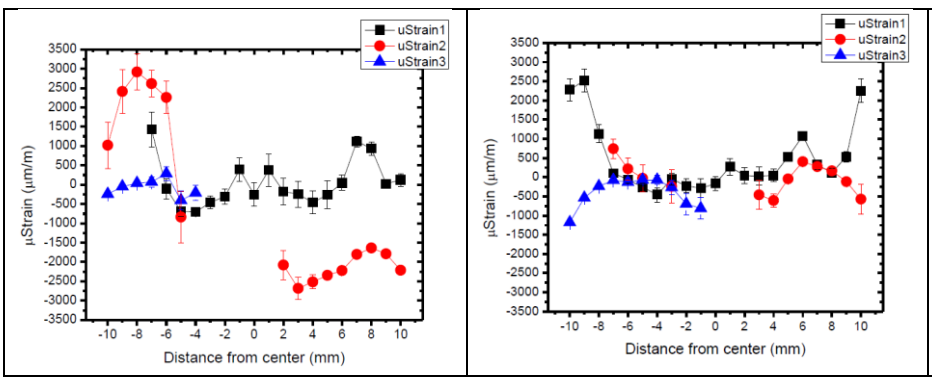

Fig. 5. Determination of the elastic strain in “spring A” (left) and “spring B” (right) springs. The notation used is: Radial = “uStrain1”, Hoop = “uStrain2”, Axial = “uStrain3”.

Microstructures in ethanol/water mixtures

Neutron Physics Laboratory - Neutron diffraction

Petr Stepanek

Proposal ID

497

Proposal ID 497

Title Microstructures in ethanol/water mixtures

A mixture of deuterated ethanol (90%) and water (10%) was prepared in 2mm quartz cells. For measurement of the background a cell filled with pure deuterated ethanol was used. Scattered intensity data were acquired with low, medium and high resolution. The scattered intensity was not too high, nevertheless the anticipated form factor of the scattering domains could be obtained. A typical result is shown in the following figure.

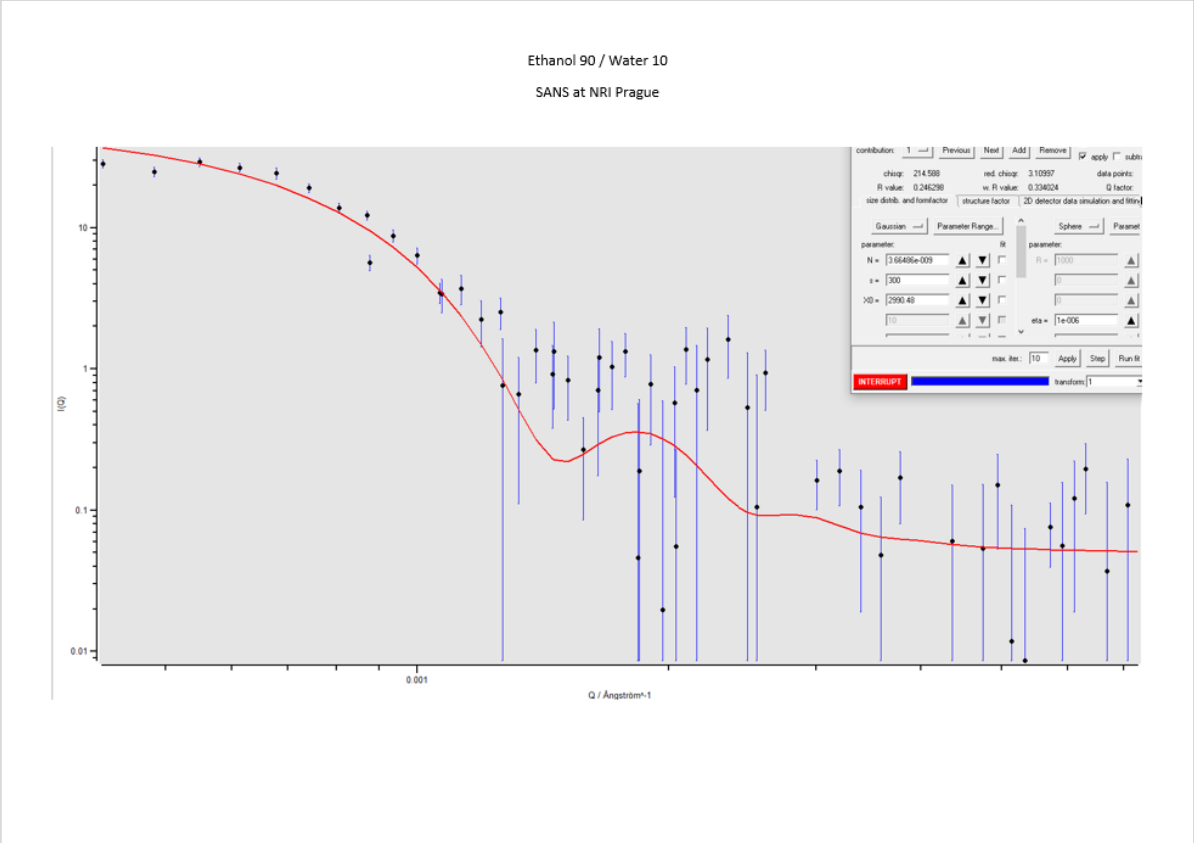

The scattering curve was fitted with a form factor of a homogeneous sphere with a Gaussian distribution of sizes, the mean size being 2990 A and distribution width 10 %.

This result is very valuable since it sets the geometrical scale of the microstructure for further investigations by various experimental techniques.

Reactions of organometallic complexes relevant for the ion beam cancer therapy

Laboratory of Cyclotron and Fast Neutron Generators

Marie Davidkova

Proposal ID

370

Report regarding proposal "Reactions of organometallic complexes relevant for the ion beam cancer therapy"

J. Kočiček, D. Reimitz, Institute of Physical Chemistry of the CAS, Prague, Czech Republic
M. Davídková, Nuclear Physics Institute of the CAS, Řež, Czech Republic

An important challenge of radiation oncology is reduction of the side effects of the treatment. Such reduction can be achieved by effective targeting of tumors by radiation using the novel ion beam techniques or by lowering the dose delivered in concomitant chemo-radiotherapy. The main advantage of such treatments is in the so-called synergistic effect, which is the enhancement of the damage delivered to the tumor over the effect of the individual chemotherapy and radiotherapy treatments.
Experimental study is exploring combined effect of organometallic compounds and ionizing radiation. Performed experiments have been focused to cisdiamminedichloridoplatinum(II) (cisP or CDDP). When irradiating plasmid DNA in solution with free molecules by ^{60}Co gamma rays, no combined effect has been observed, indicating that the contribution to DNA damage caused by products of CDDP radiolysis is negligible in comparison to the damage caused by products of radiolysis of water. After binding to DNA, CDDP adducts with DNA strongly enhance the damage in a good agreement with the results of previous studies.
To reveal potential enhancement of DNA damage induction by radiation of different quality, Tris solutions containing pBR322 plasmids have been irradiated by 30 MeV protons. Different conformations of DNA plasmid corresponding to induced DNA single and double strand breaks have been analyzed using agarose gel electrophoresis. Relative proportion of relaxed form of pBR322 corresponding to single strand break yields as a function of absorbed dose is presented in Figure 1. No modifications of DNA damage induction have been detected in samples containing cisdiamminedichloridoplatinum(II) either for low (5 mM Tris) or high (200 mM Tris) radical scavenging conditions.

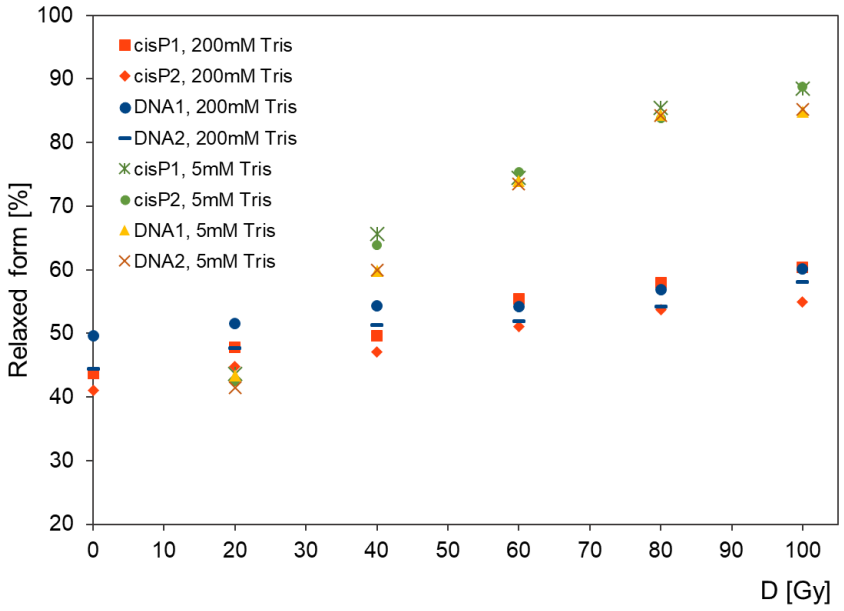

Figure 1: Proportion of relaxed form of pBR322 DNA plasmid irradiated by 30 MeV protons in presence or in absence of cisdiamminedichloridoplatinum(II) (cisP).

The work was supported by the Czech Science Foundation grant no. 16-10995Y.

Detector proton and ion response characterization for field measurements in hadron radiotherapy

Laboratory of Cyclotron and Fast Neutron Generators

Olivier Van Hoey

Proposal ID

435

Detector proton and ion response characterization for field measurements in hadron radiotherapy

Racell Nabha[1], Olivier Van Hoey[1], Cristina Oancea[2], Carlos Granja[2,3]
[1]*Belgian Nuclear Research Center (SCK-CEN), Mol, Belgium*
[2]*Advacam, Prague, Czech Republic*
[3]*Nuclear Physics Institute, Czech Academy of Sciences, Prague, Czech Republic*

Accurate characterization of the radiation field in hadron therapy is an essential step towards unraveling the radiation-induced biological effects. The MiniPIX detector is suitable for this purpose but needs to be fully characterized. The purpose of these irradiations was to test and characterize the response of our MiniPIX detector and further optimize our data processing methods and algorithms. Figure 1 shows the deposited energy and LET spectra in the detector using 31 MeV and 22 MeV proton beams during a rotation scan. Protons of lower energy (12 MeV) and other angles were also tested, but are not shown here.

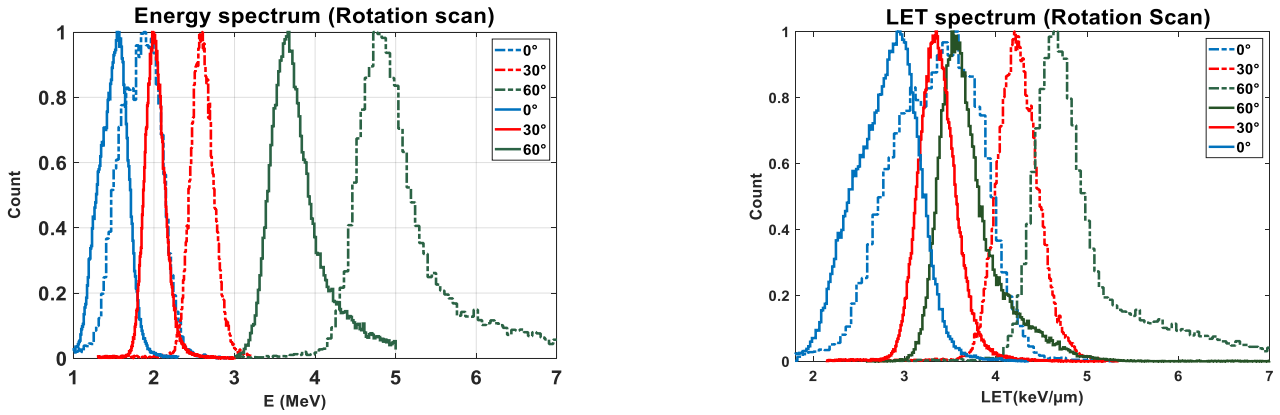

Figure 1. Deposited energy spectra (left) and LET spectra (right) for 31 MeV (solid line) 22 MeV (dashed) proton beams.

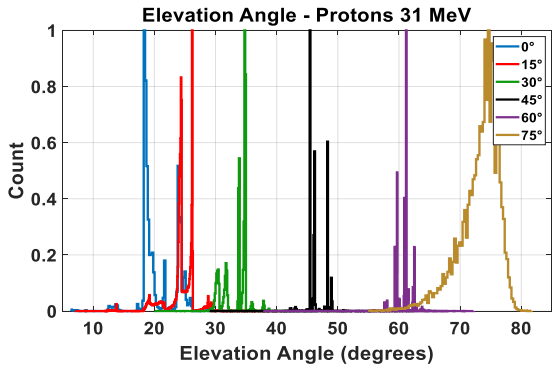

Figure 3. Reconstructed incident angle using track length and morphology.

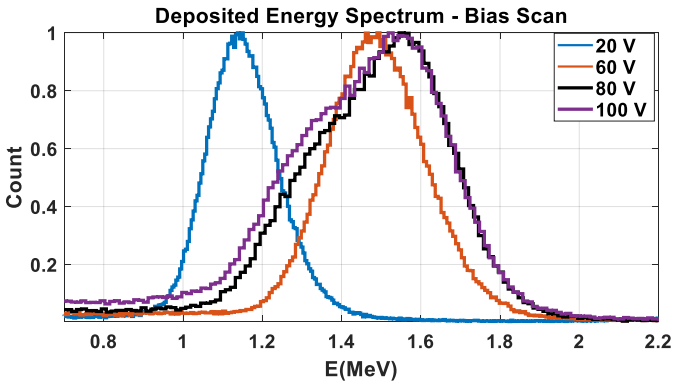

Figure 2. Energy deposition distribution for 31 MeV protons using different sensor bias at 0º incident angle.

Each particle hitting the pixelated detector will generate charge carriers along its track. Using the deposited energy and track length, the elevation angle of the incident particle can be reconstructed (figure 2). The charge sharing effect which spreads the deposited charge into adjacent pixels, depends on the sensor bias and therefore on the depleted volume. In the second part of this experiment, a bias scan was performed whereby the detector was irradiated with 31 MeV protons at the same angle and using different bias values (figure 3).

Beyond 80 V, saturation effects can be seen and signals can become strongly distorted. For our 500 um Si detector, keeping the bias at 80 V for such operations and exposures maintains the depleted volume and the charge sharing effect which lowers the per-pixel deposited charge. Monte Carlo simulations to compare and validate the results of the measurements are currently being performed.

Patterning and characterization of graphene oxide foil irradiated by Ion micro beam

Laboratory of Tandetron

Mariapompea Cutroneo

Proposal ID

371

Report

In the present proposal, the ion beam lithography technique has been used to write a line on graphene-oxide foil using the microbeam system and ions produced by a Tandetron accelerator. The depletion/enhancement of the GO components was precisely evaluated by irradiating progressively the foil and monitoring online its structural and compositional changes by RBS analysis (Figure 1).

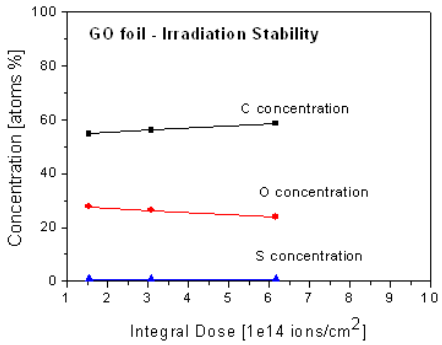

FIGURE 1. Changing of the C, O and S concentrations during the ion irradiation of the GO foils.

The agreement between RBS and SEM-EDX measurements suggests a relation between ion-irradiation fluence and oxygen reduction in GO foil and provides an essential clue that the reduction of GO can be a key factor for mobility enhancement (Figure 2).

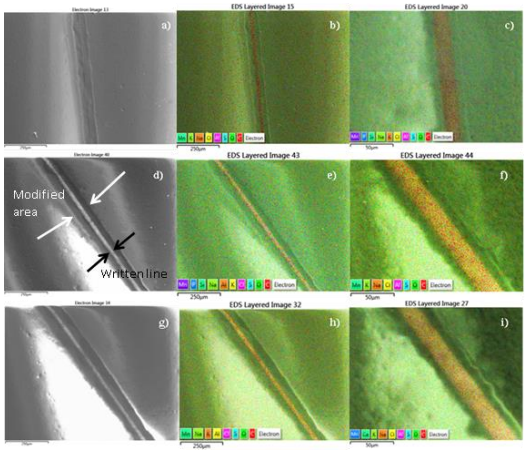

FIGURE 2. SEM images of a written line in GO foil magnified x296 and irradiated at $1.87 \cdot 10^{14}$ ions/cm^2 (a);SEM –EDX maps of the line magnified x1500 after the irradiation by$1.87 \cdot 10^{14}$ ions/cm^2 (b) and $3.75 \cdot 10^{14}$ ions/cm^2 c)

The published results reaffirm the potential of the ion- beam lithography as a promising technique for the processing of large-scale GO foil and the development of micrometric devices such as diodes and Schottky barriers as well as for other application. Further improvement of the quality along with the control of the ion-fluence irradiation to obtain the desired surface functionalisation are important challenges for the materials community but the oxidation/reduction processes need to be more fully understood to create and to tune the band gap in GO by varying the oxygen concentration.

MiniPIX neutron response characterisation for field measurements in hadron radiotherapy

Laboratory of Cyclotron and Fast Neutron Generators

Olivier Van Hoey

Proposal ID

436

MiniPIX neutron response characterization for field measurements in hadron radiotherapy

Racell Nabha[1], Olivier Van Hoey[1], Cristina Oancea[2], Carlos Granja[2,3]
[1]*Belgian Nuclear Research Center (SCK-CEN), Mol, Belgium*
[2]*Advacam, Prague, Czech Republic*
[3]*Nuclear Physics Institute, Czech Academy of Sciences, Prague, Czech Republic*

Despite the promising physical advantages of proton therapy, the dose deposited out-of-field is still unavoidable. This dose is associated with potential late effects including secondary cancers. Various particles (e.g. neutrons, photons, secondary protons, heavier ions and fragments) contribute to this dose with a wide range of physical properties and with the highest contribution coming from neutrons. The uncertainty in identifying, discriminating and characterizing these particles needs to be addressed in order to accurately estimate the physical dose delivered to normal tissues. Part of characterizing our MiniPIX detector for proton therapy applications requires assessing its response with neutrons and mixed fields.

Two sets of experiments were done during neutron irradiations. In the first one, two MiniPIX detectors (G01-500 µm Si, and I10-300 µm Si) were placed along the beam axis with different neutron converters. A neutron shield made of six PMMA targets and two aluminum targets was placed in between the detectors on a motorized shifter such that for each measurement, the beam axis, the two detectors and one of targets will be aligned. The setup is shown in figure 1a. In the second part, the PMMA and Al targets remained in place, and the two detectors were placed below the plane of the beam and 66 cm off axis , with one rotating detector and one fixed detector. The setup is shown in figure 1b.

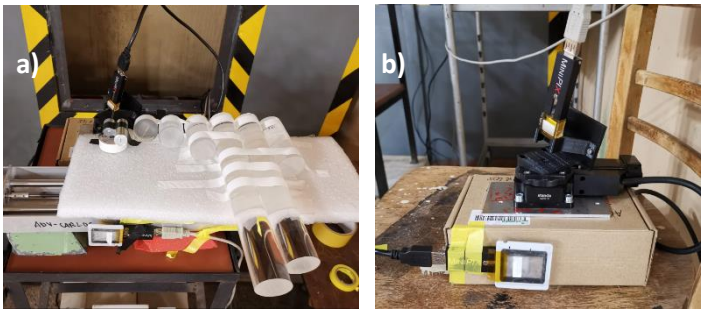

Figure 1. Setup (a) of part 1 shows MiniPIX G01 placed behind the shield and MiniPIX I10 placed in front of the shield. Setup (2) of part 2 of neutron irradiations in which G01 was rotating and I10 was fixed.

Preliminary data analysis for G01 detector shows that the total energy deposited in the detector did not significantly vary from one position (i.e. PMMA target) to the other (figure 2a). Protons having slowed down reach G01 with lower energy and hence deposit higher energy in the detector. Figure 2b shows the deposited energy spectra of recoiled protons in detector G01 compared with I10. The total number of events from recoiled protons was also reduced by a factor of 3 using the first PMMA target.

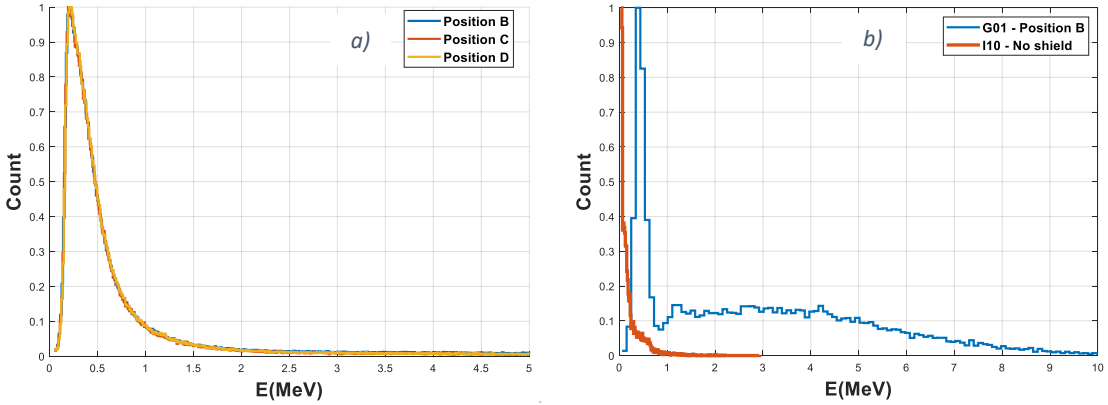

Figure 2. a) Total deposited energy spectra in G01 at 3 different positions behind the PMMA targets, and b) deposited energy spectra from recoiled protons in G01 (shielded) and I10 (unshielded).

In the majority of these measurements, the event rate and pixel occupancy were very high which led to overlapping clusters and challenging pattern recognition. The data is still being processed, and methods to improve cluster analysis and overcome the overlap are being investigated.

Study of Li ions transport in a solid electrolyte of the all-solid-state lithium ion battery

Neutron Physics Laboratory - Nuclear analytical methods with neutrons

Takane Kobayashi

Proposal ID

440

Study of Li ions transport in a solid electrolyte of the all-solid-state lithium ion battery

Takane Kobayashi, Ivo Tomandl, Jiri Vacik

In a path to a sustainable low-carbon society, conversion to renewable energy is steadily proceeding. However, the renewable energy from wind or photovoltaics fluctuates greatly, which makes it difficult to integrate it into the existing transfer grid. If an efficient electricity storage device (that would play a role of a buffer to compensate fluctuations of the energy) would exist, the speed of energy production conversion towards renewable energy would significantly accelerate. As a next generation key device for the electricity storage, a concept of all-solid-state lithium ion battery is promoted. Since the lithium ions move between the positive and negative electrodes in the active lithium ion battery, it is important for further development of the all-solid-state battery system to know how the lithium ions are distributed. It is especially important to understand how the lithium ions are behaving during the charging or discharging processes. Additionally, the issue of the interface resistance of a thin all-solid-state lithium ion battery is considered to be significant, as the resistance of the battery can be strongly affected by a lithium ion transfer.[1] We have recently investigated what happens in a separate solid electrolyte (of a thickness 150 micrometer) when a high voltage (< 15 V) is applied. The measurements were performed using the $^{6}Li(n, ^{4}He)^{3}T$ nuclear reaction. As a result, a lithium depletion layer (a considerable transfer of lithium ions between the sides of the biased thin electrolyte) has been observed (see Fig. 1). Evidently, the depletion of lithium concentration at the surface (and in a near-surface layer) is due to a delithiation process initiated by the biasing of the solid electrolyte.

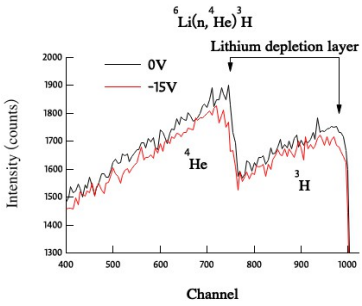

Fig. 1: ^{4}He and ^{3}T energy spectra from $^{6}Li(n, ^{4}He)^{3}T$ reaction obtained from a solid electrolyte with a thickness of 150 micrometer

Reference

1. J. Haruyama, K. Sodeyama, L. Han, K. Takada, and Y. Tateyama, Chem. Mater. 26, 4248-4255 (2014).

Changes in the compositional, structural, morphological, electrical and optical properties in elect

Laboratory of Tandetron

Mariapompea Cutroneo

Proposal ID

442

Report 442 Changes in the compositional, structural, morphological, electrical and optical properties in electrical insulator materials by ion beam**.**

Two well-established electrical insulators, graphene oxide and poly(methylmethacrylate) (PMMA) have been selectively exposed to controlled energy and fluence of ions. Ion micro beam has been proposed for processing of both graphene based material and polymeric foils for tailoring of their properties. In a single step, the mask-less production of circuit elements on graphene-oxide and poly(methylmethacrylate) was realized using a stream of 2.2 MeV alpha particles.

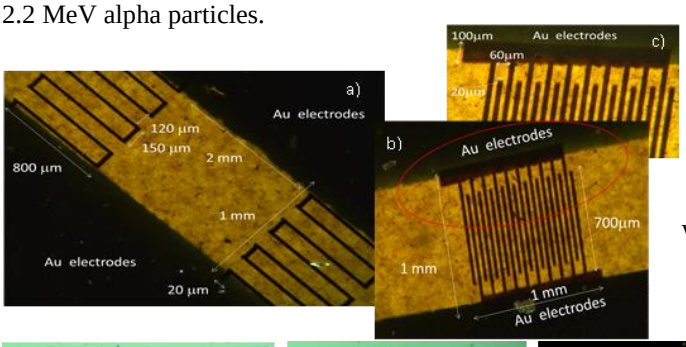

Fig. 1. Optical images 4x magnification of two resistors connected in parallel a) a large view of a capacitor b), a detail of the capacitor c) all written in graphene oxide (GO).

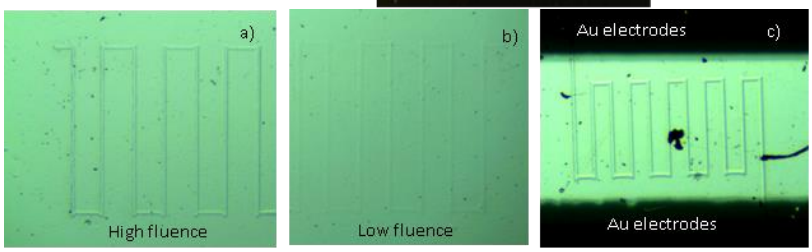

Fig. 2. Optical images resistors written at $3.8 \cdot 10^{13}$ ions/cm^2 a) at $3.7 \cdot 10^{14}$ ions/cm^2 b) a resistor written between two electrodes at $3.7 \cdot 10^{14}$ ions/cm^2 c) all written in PMMA.

Fig.2a reports swelling and shrinking and the contour have a glassy-appearance of the irradiated areas in PDMS. Since the glass transition of PMMA occurs at about 105° maybe the thermal degradation and deformation effects took place and the gas diffusion is not predominant any more. **Fig.2b** shows no swelling and shrinking maybe because as decreasing the size of the irradiated surface, the PMMA bears higher ion fluences because the related sheer stress will also be small and higher ion fluence can be applied.

The induced deoxygenation, and dehydrogenation change the compositional, structural and electrical properties in the exposed samples. The accuracy of the method has been investigated by Rutherford backscattering spectrometry, elastic recoil detection analysis as reported in Table I.

SAMPLE	*COMPOSITION OF THE FOILS (at %)*							
GO 7 µm	C	O	H	S	Mn	Ca	C/O	H/O
Pristine	52.5	27.1	19.7	0.65	0.05		1.94	0.73
Irradiated by 2.2 MeV He^{2+} ions at $6.4 \cdot 10^{14}$ ions/cm^2	56.7	23.8	16.0	0.65	0.05		2.14	0.60
Irradiated by 2.2 MeV He^{2+} ions at $1.1 \cdot 10^{15}$ ions/cm^2	60.4	26.9	14.9	0.65	0.05		2.54	0.63
PMMA 50 µm	C	O	H	S	Mn	Ca	C/O	H/O
Pristine	59.9	14.7	25.2			0.04	4.07	1.71
Irradiated by 2.2 MeV He^{2+} ions at $3.8 \cdot 10^{13}$ ions/cm^2	65.9	13.3	20.5			0.06	4.95	1.54
Irradiated by 2.2 MeV He^{2+} ions at $3.7 \cdot 10^{14}$ ions/cm^2	71.9	11.4	16.7			0.07	6.31	1.46

Table I Composition of GO foils un-irradiated and irradiated by 2.2 MeV Helium ions with 6.4 x 10^{14} ions/cm^2 and 1.15 x 10^{15} ions/cm^2 and of PMMA foils un-irradiated and irradiated by 2.2 MeV Helium ions with 3.8 x 10^{13} ions/cm^2 and 3.7 x 10^{14} ions/cm^2.

The shrinking is connected to the diffusion of gas during and after the ion irradiation. Shrinking decreases with the ion fluence because the incoming ions hit the already modified region and the amount of gas molecules decreases due to desorption in vacuum and the successive energy deposition occurs producing minor scission processes and cross-linking of radicals. Raman spectroscopy on GO indicated the generation of defects and structural modification as a consequence of the ion irradiation. Electrical measurements on the insulators indicated a significant reduction of resistivity on GO and a slight change in its electrical properties increasing the fluences of irradiating ions. In GO the deoxygenation of the foil induces a restoration of the electrical properties of graphene, while in PMMA the ion irradiation induces irreversible changes in its molecular structure by generation of chain scission, crosslinking and carbonization.

The present work is addressed to a design of direct–patterning of circuits or optical guides which are extensively used in soft electronic for the realization of flexible and stretchable electronics and in microelectronics.

Study of structural properties of MAX/MX phase thin films synthetized by ion beam sputtering

Laboratory of Tandetron

Giovanni Ceccio

Proposal ID

445

Report regarding the proposal "Study of structural properties of MAX/MX phase thin films synthetized by ion beam sputtering"

G. Ceccio, P. Horak, A. Cannavò

Nucl. Physics Inst., Rez, Czech Republic

MAX phases are ternary carbides or nitrides with the formal stoichiometry formula of Mn+1AXn (n = 1, 2, 3), where M is representative of an early-transition d metal (i.e., Sc, Ti, V, Cr, Zr, Nb, Mo, Hf, and Ta), A is an element from (mainly) the IIIA or IVA group (i.e., Al, Si, P, S, In, Sn, and Pb), and X is either carbon or nitrogen. The properties of the MAX and MXene systems are based on combination of the best attributes of the metals and ceramics. For example, MAX phases are resistant to radiation, thermal shock or corrosion and exhibit high electrical conductivity. Thin films of MAX and MXene phases were prepared by ion beam sputtering followed by thermal annealing in vacuum. The thickness, composition and stoichiometry of the films were analyzed by the Rutherford Back-scattering method (RBS) and Nuclear Resonance Analysis (NRA) using α-particles with an energy of 2000 keV and 3.046, 4.280 keV for RBS and NRA, respectively. The measurements were carried out at the Tandetron 4230 MC accelerator at NPI (CANAM infrastructures). Important results were obtained studied the MAX phases: Ti_3InC_2 and Ti_2SnC (see Fig. 1)

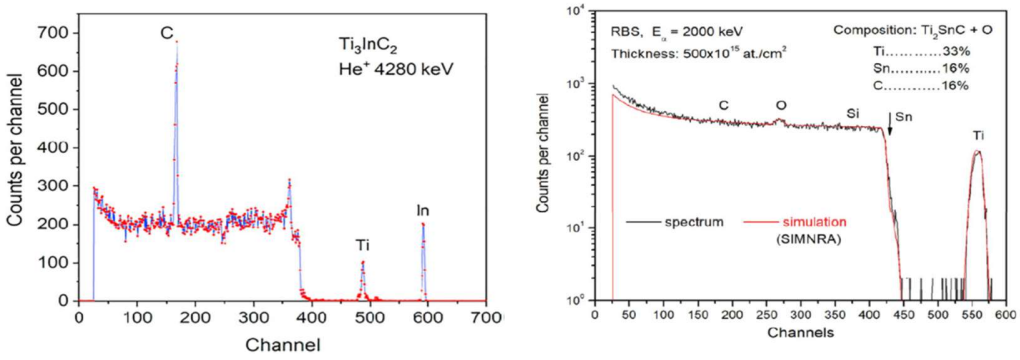

Figure 1 The NRA spectra of the Ti3InC2 film showing the C resonance analysis at 4280 keV(left) IBA analysis of the Ti2SnC thin film: RBS using 2 MeV alpha particles (right)

The data concerning the preparation of the MAX phase thin films by ion sputtering were partially published [1,2], but other results concerning the modification of the thin films by ion implantation are still under evaluation for future publications.

[1] Surface and Coatings Technology Volume 394, 25 July 2020, 12583
[2] RADIATION EFFECTS & DEFECTS IN SOLIDS 2020, VOL. 175, NOS. 1–2, 177–189

Testing and calibration of MIRAM spacecraft radiation monitor for ESA

Laboratory of Cyclotron and Fast Neutron Generators

Adam Smetana

Proposal ID

446

MIRAM at proton beams in CANAM

CANAM Cyklotron Report experiment LPC MIRAM, Sept. and Dec. 2019, Milan Malich – IEAP CTU Prague

We have performed measurements in two stages in September and in December 2019. The spectrometric response and SEU analog processing chain was tested of the MIRAM device and his LPC part. Miram LPC device is small, low-power radiation monitor for Space. It is composed from 300um 4xSi diodes (in tested device only one was assambled).

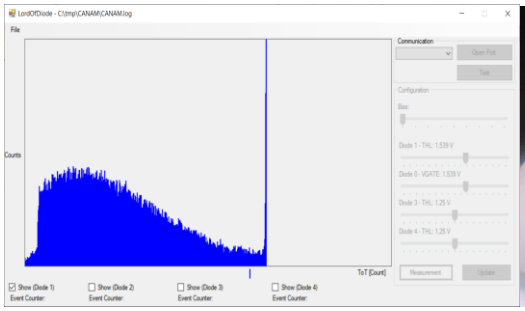

Figure 1: Histogram of Time over Threshold from Diode

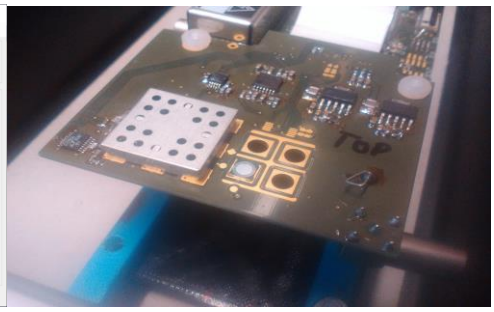

Figure 2: Analog Front End V

Device was tested in energy range 8 to 31MeV. Energy deponed by particle is converted to Time over Threshold (ToT) value. Result is histogram Time over Threshold values. Broad peak is energy of Beam 8MeV due pile up effect on Si diode and second thin peak is saturation peak of ADC. During Beam proton test no mallfunction caused by SEU was not observed.

Report z měření na cyklotronu Peter Rubovič, ÚTEF ČVUT v Praze

Dne 10.12.2019 proběhlo měření v cyklotronové laboratoři ÚJF AV ČR v Řeži. Měřili jsme úhlovou závislost odezvy 3D trasovače částic vyvinutého firmou Advacam ve spolupráci s ÚTEF ČVUT v Praze, který sestává z čtveřice hybridních pixelových detektorů Timepix s 300 µm tlustými křemíkovými sensormi a ztenčeními readout chipmi o tloušťce 100 µm, které jsou na sebe nalepeny. Měření proběhlo s protony o energii 35 MeV. Výstupem měření je ověření funkčnosti detektoru a vytvoření ukázky pro akademické a obchodné partnery. Na měřených datech lze pozorovat profil depozice energie protonů v sensoru. Tato informace může být využita například pro monitorování toku primárních i sekundárních částic v hadronové terapii při kalibraci generátoru částic.

CANAM Cyklotron Report experiment ACQP MIRAM, Dec. 2019, Carlos Granja, Cristina Oancea- ADVACAM Prague

The spectrometric and particle tracking response of the MIRAM ACQP BB Timepix-3 hybrid semiconductor Si sensor 500 µm for charged particle detection was tested with proton beams with energies ranging from 12 to 31 MeV, see Fig 1. Bias and rotation and scans were performed, see Fig. 2. The purpose was to examine the LET-response and tracking resolving power to high-LET particles (protons near the Bragg peak).

The pixel detector TPX3 ASIC chip provides quantum–imaging sensitivity and visualizes the track of each individual particle and its 3D direction, allowing LET determination over a wide LET range (0.1 – 100 keV/µm) for incoming particles under various angles. Results include per-pixel energy deposition (loss) and linear energy transfer (LET) at varying incident directions, see Fig.3.

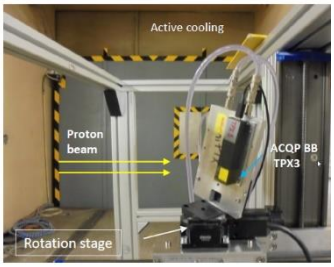

Figure 1. Experimental setup at the Cyklotron U-120 NPI, Rez. The ACQP BB TPX3 device was placed on a rotation stage and irradiated under several angles with tunable protons.

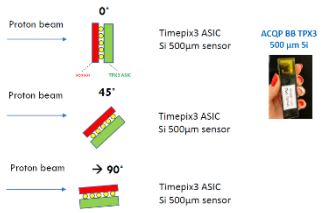

Figure 2. Schematic representation of the rotation scan using ACQP BB TPX3.

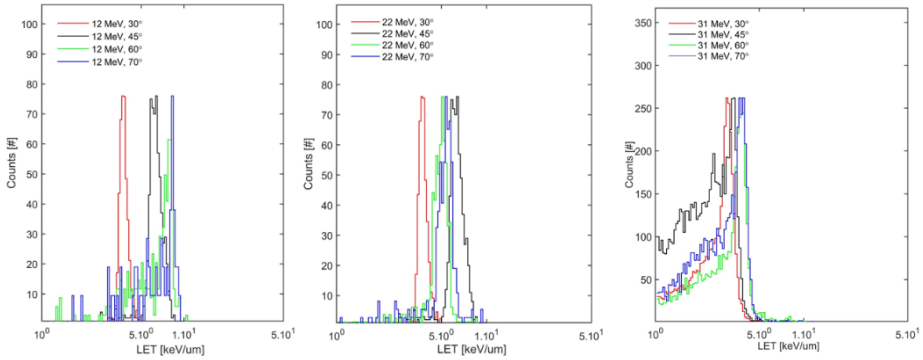

Figure 3. LET spectra measured with the Timepix–3 ACQP for a) 12 MeV, b) 22 MeV and c) 31 MeV proton beam. The data are displayed for measurements in air at: 30° (red), 45° (black), 60° (green) and 70° (blue) incident directions. The deposited energy, and LET, vary, namely near the Bragg peak.

SINE2020 feasibility study - DED sample residual stress measurement

Neutron Physics Laboratory - Neutron diffraction

Pavel Strunz

Proposal ID

449

Measurements in Direct Energy Deposition (DED) sample for FEM method check

Residual stress is a side effect of a Direct Energy Deposition (DED) processes. Understanding the phenomena allows choosing suitable deposition strategy to reduce residual stress and shape distortion. A FEM modelling of the DED process and other experimental method can evaluate residual stress distribution but those methods needs to be compared to known reference to provide correct results.

A cubic sample from stainless steel 316L deposited on InssTek MX600 DED device is investigated and residual stress and porosity are evaluated by software and lab technique usually available.

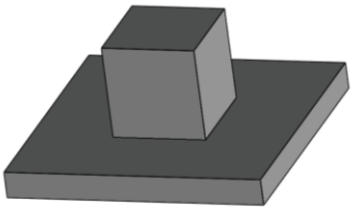

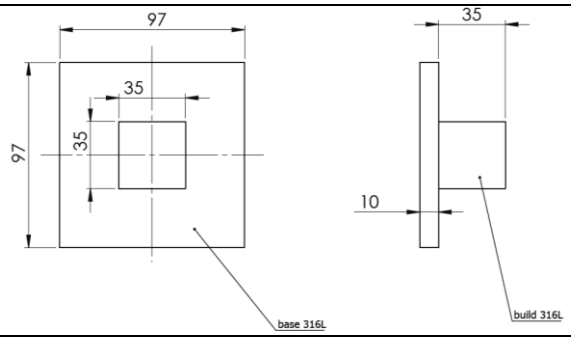

Scheme of the cubic sample made of stainless steel 316L

The incident and diffracted beam are formed by 5×5 mm^2 and 5 × open cadmium slits, respectively. To determine the three strain components, different geometrical arrangements of the examined specimen with respect to the scattering vector were performed.

The measured maximum compressive stresses correspond always to the z direction, being close to -400 MPa. A maximum tensile stress of ~ 100 MPa is found close to the top surface at line x=10 in y direction. The central region around the symmetry axis and around the z=12 line undergo compressive stresses.

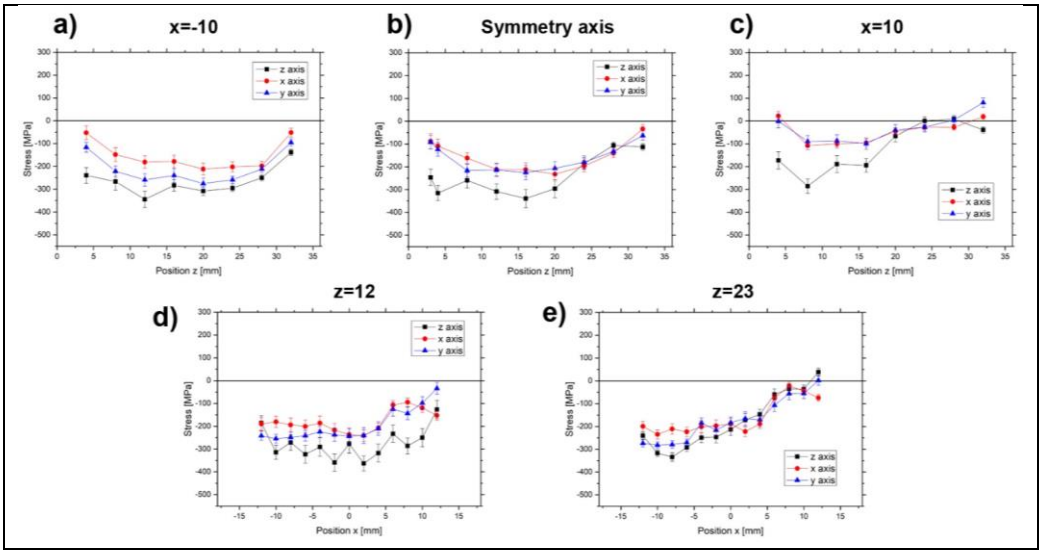

Residual stresses for the vertical lines at a) x=-10, b) x=0 and c) x=10 and for the horizontal lines at d) z=12 and e) z=23.

Residual stress measurement has shown that

- Maximum compression and tensile stresses are ~ -400 MPa and 100 MPa, respectively.
- Central region is confirmed to be under compression.
- Stresses do not mirror around the symmetry axis.
- Regions close to the top surface exhibit more asymmetry in the residual stresses, probably as a consequence of the distorted sample.

SINE2020 feasibility study - DED sample porosity measurement

Neutron Physics Laboratory - Neutron diffraction

Pavel Strunz

Proposal ID

450

Measurements in Direct Energy Deposition (DED) sample for FEM method check - porosity measurement

Residual stress is a side effect of a Direct Energy Deposition (DED) processes. Understanding the phenomena allows choosing suitable deposition strategy to reduce residual stress and shape distortion. A FEM modelling of the DED process and other experimental method can evaluate residual stress distribution but those methods needs to be compared to known reference to provide correct results. Porosity can influence the microstructure of the material and correspondingly also the modelling parameters.

A 2 mm slices cut from the original DAD cubic sample from stainless steel 316L deposited on InssTek MX600 DED device were investigated by SANS, and porosity was evaluated.

Measured data

The sample and its subsrate of the same material were scanned in several points. Some of the measured data are shown in the figure Fig. SANS5:

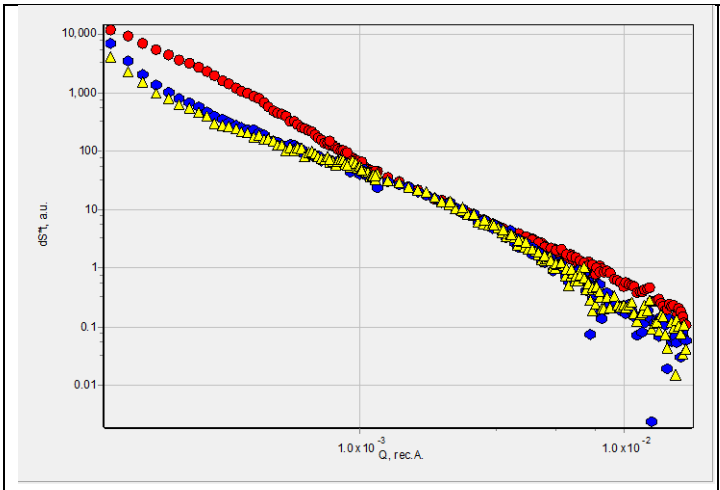

Fig. SANS5. Scattering for studied areas F (red spheres), H (blue hexagons) and L (yellow triangles).

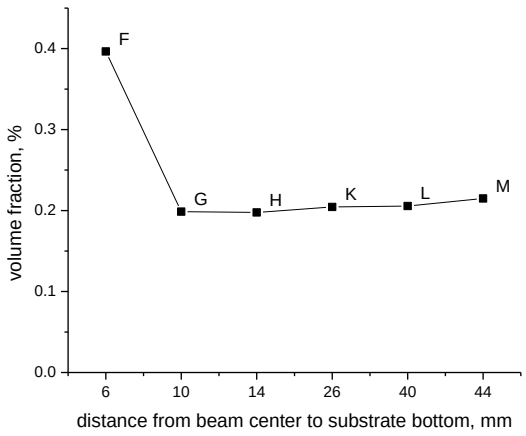

Fig. SANS6. Porosity volume fractions (small particles) as function of distance from sample side (area F – is substrate, G – partially substrate and studied material, K – is center of the sample).

For evaluation, model of spheres was used, using 2 log-normal size distributions – for small and large particles.

Although, SANS data for the locations H, K, K and M are alike, locations H and G showed rather higher intensity mostly in low Q ($<10^{-3}$ Å^{-1}) region (see Fig. SANS5). The SANS results showed that porosity (or other scattering objects) in substrate (point F) has about twice larger fraction (0.4%) for small particles model in comparison with deposited material (0.19-0.21%) (Fig. SANS6).

Conclusions

SANS measurement led to the conclusions:

- Scattering curves measured in deposited part of the sample are alike within statistical error. These data were fitted by spherical model assuming that scattering objects are pores. Fitted volume fraction of porosity (small particles model part) is about 0.2%, mean radius of pores ≈100 nm.
- Azimuthal scan didn't show any anisotropy in plane of the sample.

SINE2020 feasibility study - DED sample texture measurement

Neutron Physics Laboratory - Neutron diffraction

Pavel Strunz

Proposal ID

451

Measurements in Direct Energy Deposition (DED) sample for FEM method check

Residual stress is a side effect of a Direct Energy Deposition (DED) processes. Understanding the phenomena allows choosing suitable deposition strategy to reduce residual stress and shape distortion. A FEM modelling of the DED process and other experimental method can evaluate residual stress distribution but those methods needs to be compared to known reference to provide correct results. Important part of the microstructural modelling is the texture.

A cubic sample from stainless steel 316L deposited on InssTek MX600 DED device was investigated and texture was evaluated by software available in the lab.

Experimental Pole Figures

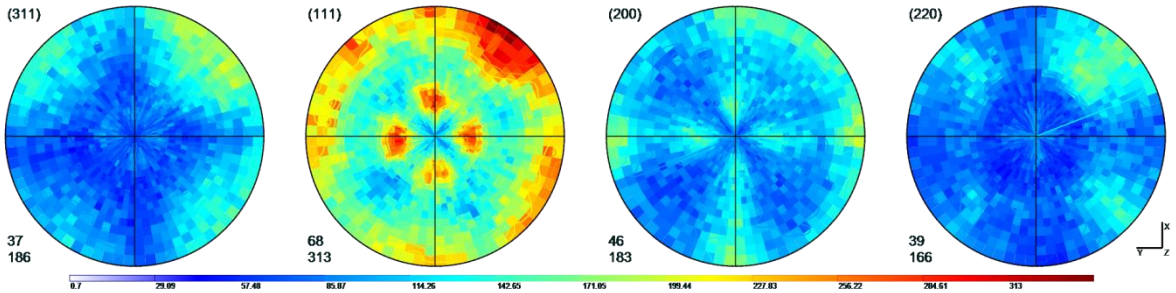

Calculated Pole Figures

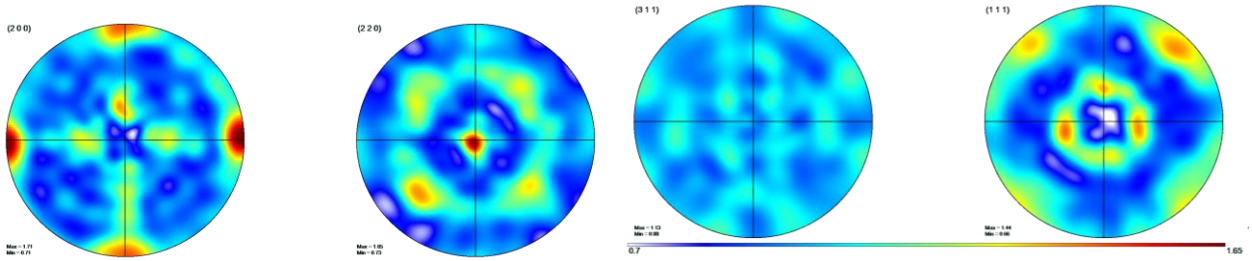

Inverse Pole Figures

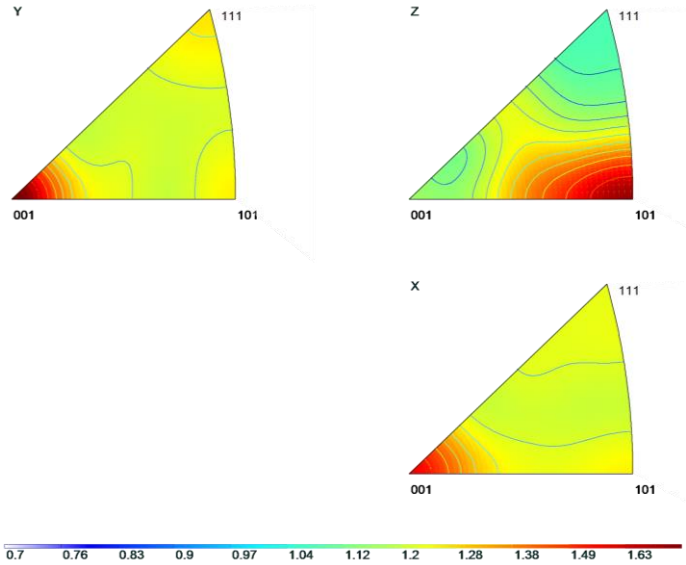

Conclusions

Texture measurement using neutron diffraction revealed that

- 110 crystallographic direction is preferably in Z direction (i.e. perpendicular to base plate)
- X and Y direction are qualitatively the same: 100 directions of crystallites are preferably parallel to them
- However, X direction texture is weaker (max. 1.44, min 0.94 in the inverse pole figure), Y direction is stronger (max. 1.68, min 0.94)

RBS characterisation of ScN thin films compositions

Laboratory of Tandetron

Jan Lancok

Proposal ID

389

Joris More Chevaliet, RNDr. Anna Macková, Ph.D. **at all.**
Institute of Physics AV CR, Na Slovance 2, 182 21 Prague 8, Czech Republic, Nuclear Physics Institute of the ASCR, v. v. i., Rez 130, 250 68, Rez near Prague, Czech Republic

ScN/MgO

The ScN layers were deposited on double-side polished MgO (001) substrate in an ultra-high-vacuum (UHV) system (10-8 Pa) by DC reactive magnetron sputtering using a 99.9999% pure N2 discharge. The sample holder was electrically heated to reach the temperature of 700 °C. The working pressure of 3.5 Pa was used to sputter ScN from 99.9% pure Sc target of one inch diameter with a detectable contaminant of Ta at 0.1%. The thickness was measured using a Profilometer and confirmed by spectroscopic ellipsometry.

Experimental details

The measurements were performed by using the ion beam provided by the tandem accelerator, Tandetron MC 4130, at the Nuclear Physics Institute in Rez near Prague. A typical RBS spectrum you can see in Figure 2.

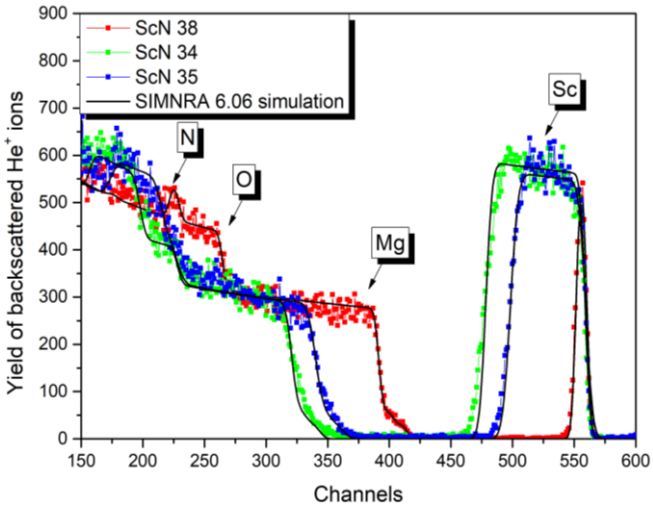

Figure 2: The RBS-C measurement of ScN/MgO measured by energy 2.0 MeV using He^+ ions.

Results

In Table 1 you can see in the second column name of the sample, third – thickness *t* from elipsomentry (in nm unit). In columns 4 and 5, there are *t* of each samples from RBS mentioned in 1e15at./cm^2 unit and nm (calculated at density 4.28(2) g/cm^3). In columns 6-10, there are concetrations of Sc, N, C Mg and O (mentioned in atomic percent) determined using the RBS method.

Table 1: Samples concentration

n.	sample	*t* (elipsometry) [nm]	*t* (RBS) [1e15at./cm^2]	*t* (RBS) [nm]	Sc [at.%]	N [at.%]	C [at.%]	Mg [at.%]	O [at.%]
1.	ScN 38	32	230	24	42.0	52.0	6.0	50	50
2.	ScN 34 700°C	248	2100	217	41.0	53.5	5.5	50	50
3.	ScN 35 700°C	190	1620	169	39.5	57.0	3.5	50	50

The received data will be used for publication concerning ScN thin films and compare with those obtained from EDX, XPS and XRF

Characterisation of detectors response in heavy charged particle beams

Laboratory of Cyclotron and Fast Neutron Generators

Iva Ambrožová

Proposal ID

453

Report regarding proposal “Characterisation of detectors response in heavy charged particle beams”

Iva Ambrožová and Martin Kákona
Nuclear Physics Institute, Czech Academy of Sciences, Czech Republic

Si-diode based detectors have been used for measurements onboard aircraft and spacecraft for many years. Recently at our department, new open source Si-diode based spectrometers Airdos and Spacedos have been developed. Airdos is used for long-term measurements onboard aircraft, Spacedos is intended for measurements onboard spacecraft and satellites. To determine dosimetric characteristics such as absorbed dose, proper calibration is needed, which is usually based on the irradiation of detectors in various radiation beams.
Using the cyclotron proton beam with initial energy of about 35 MeV together with Al degraders, we obtained several calibration points. Spectra of deposited energy measured with Spacedos is shown in Figure 1, an example of a calibration curve for Spacedos is shown in Figure 2.

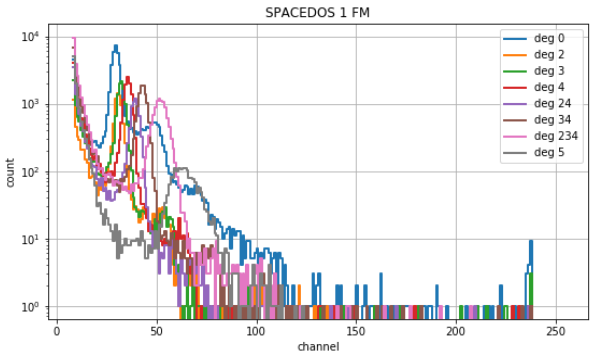

Fig. 1. Energy deposited spectra measured with Spacedos

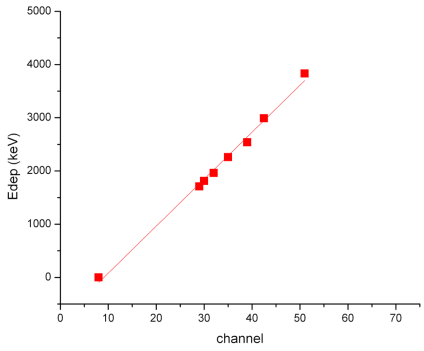

Fig. 2. Calibration curve for Spacedos

Reference

M. Kákona, Research on cosmic rays on board aircraft using a newly developed PIN diode detector, PhD thesis, CTU in Prague, 2020.
M. Kákona et al. AIRDOS - open source PIN diode airborne dosimeter, to be submitted to JINST, 2020.

Damage formation and optical activation of dopants in ZnO

Laboratory of Tandetron

Romana Mikšová

Proposal ID

393

Report regarding proposal "Damage formation and optical activation of dopants in ZnO."

A.Macková, P.Malinský, A.Jagerová, R.Mikšová, Nuclear Physics Institute of the Czech Academy of Sciences, v. v. i., Rez, Czech Republic
P.Nekvindová, J.Cajzl, Department of Inorganic Chemistry, Institute of Chemical Technology, Prague, Czech Republic
R. Böttger, S. Akhmadaliev, Institute of Ion Beam Physics and Materials Research, Helmholtz Zentrum Dresden-Rossendorf, Dresden, Germany

In our results, the structural modification of ZnO in c-plane (0001), a-plane (11–20) and m-plane (10-10) ZnO – implanted with Au^+ ions using the energy of 400 keV and fluences of 5×10^{14} and 1×10^{15} cm^{-2} and subsequently annealed at 600°C in O_2 was investigated. Deep structural damage grew with increased Au-ion fluence and Au did not exhibit strong out-diffusion from the depth to the surface during the post-implantation annealing. RBS measurements during ion implantation revealed more progressive deep-damage formation in the c- and m-planes than in the a-plane ZnO. Simultaneously, the smallest Zn sub-lattice disorder deduced from RBS/C measurements was observed in the a-plane ZnO. During post-implantation annealing, a slight structure recovery (about 4%) was observed in all orientations.

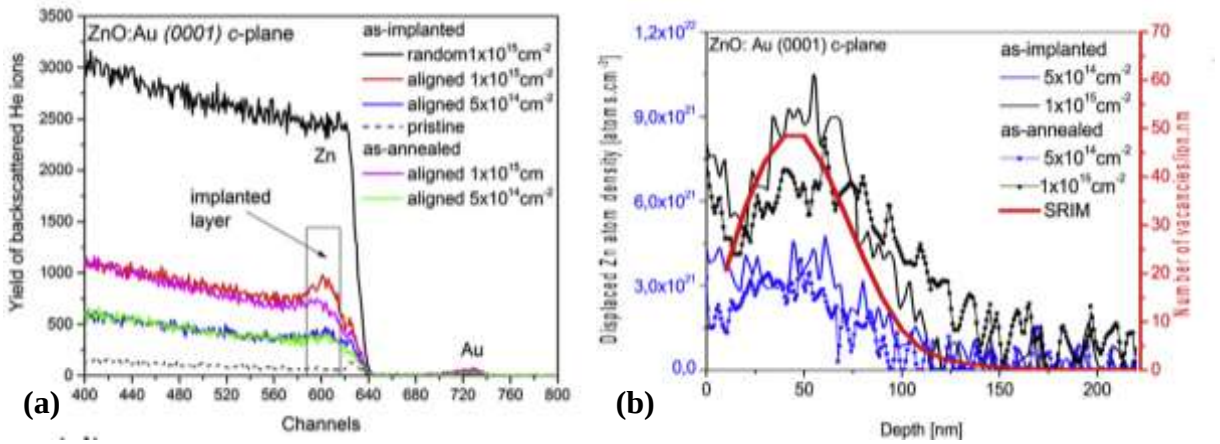

Figure 1. The RBS/channelling spectra for as-implanted and as-annealed samples: (a) c-plane ZnO. The region of interest appropriate to the ion-implanted layer is indicated in the black rectangle. The density profiles of the displaced Zn atom for various ion-implantation fluences determined from RBS/C spectra for as-implanted and as-annealed samples for the c-plane (b). SRIM-predicted Zn vacancy depth-distribution profiles are shown.

Raman spectroscopy confirmed the increasing structure disorder with the enhanced ion fluence for all as-implanted ZnO orientations and a partial reconstruction of the ZnO structure during annealing when the intensity of E_2 phonons was increased and that of longitudinal optical (LO) phonons was suppressed because of the disorder recovery. E_2(high) and E_1(LO) Raman phonon modes show a significant modification mainly in the m-plane.

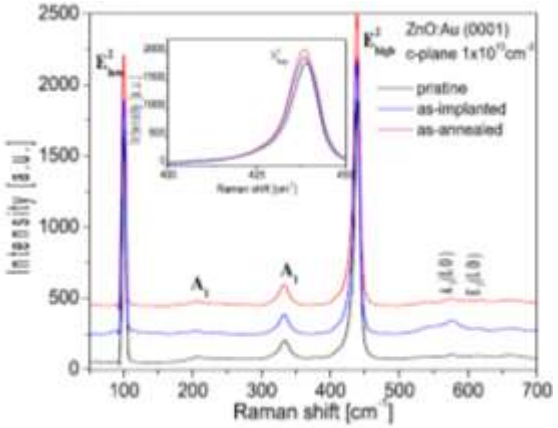

Figure 2. The Raman spectra of as-implanted (blue curves) and as-annealed (red curves) samples implanted using the ion-implantation fluence of 1×10^{15} cm−2 for c-plane ZnO.

All results from experiments on ZnO were published in Vacuum, Nuclear Instruments and Methods in Physics Research B and Journal of Alloys and Compounds.